J. Plasma Phys. (2022), *vol*. 88, 905880606
Published by Cambridge University Press

doi:10.1017/S0022377822001131

On the control of electron heating for optimal laser radiation pressure ion acceleration

H.-G. Jason Chou [1,2,†], **Anna Grassi** [1], **Siegfried H. Glenzer** [1] **and Frederico Fiuza** [1,†]

[1]High Energy Density Science Division, SLAC National Accelerator Laboratory, Menlo Park, CA 94025, USA

[2]Department of Physics, Stanford University, Stanford, CA 94305, USA

(Received 19 July 2022; revised 21 October 2022; accepted 24 October 2022)

We study the onset of electron heating in intense laser–solid interactions and its impact on the spectral quality of radiation pressure accelerated ions in both hole boring and light sail regimes. Two- and three-dimensional particle-in-cell (PIC) simulations are performed over a wide range of laser and target parameters and reveal how the pulse duration, profile, polarization and target surface stability control the electron heating, the dominant ion acceleration mechanisms and the ion spectra. We find that the onset of strong electron heating is associated with the growth of the Rayleigh–Taylor-like instability at the front surface and must be controlled to produce high-quality ion beams, even when circularly polarized lasers are employed. We define a threshold condition for the maximum duration of the laser pulse that allows mitigation of electron heating and radiation pressure acceleration of narrow energy spread ion beams. The model is validated by three-dimensional PIC simulations, and the few experimental studies that reported low energy spread radiation pressure accelerated ion beams appear to meet the derived criteria. The understanding provided by our work will be important in guiding future experimental developments, for example for the ultrashort laser pulses becoming available at state-of-the-art laser facilities, for which we predict that proton beams with ∼150–250 MeV, ∼30 % energy spread, and a total laser-to-proton conversion efficiency of ∼20 % can be produced.

Key words: intense particle beams, plasma simulation, plasma instabilities

1. Introduction

In the last two decades, there has been a significant effort in exploring the generation of high-energy (1–100 MeV) ion beams in plasmas produced by intense ($I > 10^{18}$ W cm^{-2}) laser–solid interactions (Daido, Nishiuchi & Pirozhkov 2012; Macchi, Borghesi & Passoni 2013). It has been shown that accelerating gradients as high as teravolts per metre can be created in the plasma (Wilks *et al.* 2001) and ion beams can be produced with

† Email addresses for correspondence: jasonhc@slac.stanford.edu, fiuza@slac.stanford.edu

small emittance ($< 0.1\pi$ mm mrad (Borghesi *et al.* 2004; Cowan *et al.* 2004)) and short bunch duration ($\lesssim$1 ps (Dromey *et al.* 2016)). These promising results and the potential to produce high-energy, high-current ion beams in more compact systems than solid-state-based accelerators (Cahill *et al.* 2018) make the study of laser-driven ion acceleration an active area of research.

Laser-driven ion beams are now routinely used for radiography of high-energy-density plasmas (Borghesi *et al.* 2002; Rygg *et al.* 2008) and hold promise for applications in isochoric heating of materials (Patel *et al.* 2003; Tahir *et al.* 2005), fast ignition of inertial confinement fusion (Roth *et al.* 2001), injectors for conventional accelerators (Antici *et al.* 2008; Aymar *et al.* 2020) and tumour therapy (Bulanov *et al.* 2008; Kraft *et al.* 2010; Loeffler & Durante 2013; Bulanov *et al.* 2014; Linz & Alonso 2016; Kroll *et al.* 2022). Important requirements for many of these applications are the ability to produce controllable, quasimonoenergetic (low energy spread) ion beams and at a high-repetition rate. These remain significant challenges for laser-driven ion beams, despite the progress in exploring different acceleration mechanisms, and significant developments in high-repetition rate targets (Kim, Göde & Glenzer 2016; Gauthier *et al.* 2017; Göde *et al.* 2017; Obst *et al.* 2017; Curry *et al.* 2020).

The most studied laser-driven ion acceleration mechanism to date – both theoretically and experimentally – is the target normal sheath acceleration (TNSA) (Snavely *et al.* 2000; Wilks *et al.* 2001; Mora 2003). Hot electrons are produced near the front surface of the target during the laser–plasma interaction, typically via $\boldsymbol{J} \times \boldsymbol{B}$ (Kruer & Estabrook 1985; May *et al.* 2011) and Brunel (vacuum) heating (Brunel 1987) mechanisms, which are maximized for linearly polarized lasers (Wilks & Kruer 1997; Gibbon 2005). These hot electrons cross the dense target and escape into the vacuum on the rear side, setting up a strong space-charge sheath field that accelerates the target ions from the back surface in the target-normal direction. Ion beams produced by this mechanism are laminar and possess small emittance, however, their energy spectrum is very broad, being typically characterized by an exponentially decreasing energy distribution (Snavely *et al.* 2000; Wilks *et al.* 2001; Mora 2003).

Alternative ion acceleration schemes have been proposed in order to produce more narrow (quasimonoenergetic) ion spectra, including collisionless shock acceleration (CSA) (Denavit 1992; Silva *et al.* 2004; Fiuza *et al.* 2012; Haberberger *et al.* 2012) and radiation pressure acceleration (RPA) (Wilks *et al.* 1992; Esirkepov *et al.* 2004; Macchi *et al.* 2005; Robinson *et al.* 2008). Collisionless shock acceleration relies on the reflection of ions off a moving electrostatic shock front produced by the laser–plasma interaction near the front surface, which travels at roughly a constant speed inside the target. A small fraction ($\simeq$ 1 %–10 %) of the bulk ions is reflected by the shock producing a narrow energy spread ion beam. Hot electrons are important for driving the ion-acoustic waves that mediate shock formation inside the target, and therefore TNSA will also naturally accompany CSA, which can inadvertently broaden the ion spectrum. Specific shaping of the target density has been proposed as a way to control TNSA and produce high-quality beams from CSA (Fiuza *et al.* 2012, 2013). Recently, tuning of the plasma density profile using a second laser was shown to produce narrow energy spread ion beams from CSA (Pak *et al.* 2018). However, achieving precise control of the plasma density profile remains a challenge.

Radiation pressure acceleration relies on the slowly varying, cycle-averaged component of the ponderomotive force exerted by the intense laser pulse on the electrons at the front surface of the solid target. It is this radiation pressure that creates a charge separation between the electrons and the ions that accelerates the latter. It can potentially result in the generation of a quasimonoenergetic and laminar ion beam, provided that the

https://doi.org/10.1017/S0022377822001131 Published online by Cambridge University Press

accelerating structure is maintained stable and with uniform velocity, similarly to the case of CSA. In theory, RPA can produce ion beams with very high density because almost all ions in the laser focal region can be accelerated by the space-charge field. However, the experimental characterization of this acceleration scheme and observation of narrow energy spread ion beams have been challenging (Henig *et al.* 2009; Palmer *et al.* 2011; Kar *et al.* 2012; Steinke *et al.* 2013; Bin *et al.* 2015; Scullion *et al.* 2017; McIlvenny *et al.* 2021). An important difficulty relies on the requirement of low electron heating for efficient momentum transfer from the laser to the ions, and to avoid other competing ion acceleration mechanisms, such as TNSA and CSA, to develop and dominate. Indeed, recent experiments producing nearly 100 MeV proton beams likely involved the combination of different acceleration schemes and the observed energy spectra were broad (Kim *et al.* 2016; Wagner *et al.* 2016; Higginson *et al.* 2018; Shen *et al.* 2021). Other significant challenges include the mitigation of corrugations at the laser–target interaction surface arising due to instabilities (Palmer *et al.* 2012; Eliasson 2015; Sgattoni *et al.* 2015; Wan *et al.* 2020; Chou *et al.* 2022) and finite laser spot effects (Klimo *et al.* 2008; Dollar *et al.* 2012) and the control of the preplasma level that is naturally formed from the preheating and expansion of the target by a laser prepulse, which poses significant constraints on the laser contrast (Varmazyar, Mirzanejhad & Mohsenpour 2018).

In all these laser-driven ion acceleration schemes electron heating plays a major role in controlling the dominant acceleration mechanism and the quality of the accelerated ion beams. While it is well established that the laser polarization – linear versus circular – can be important in controlling electron heating via the $\boldsymbol{J} \times \boldsymbol{B}$ mechanism (e.g. May *et al.* 2011), it is not clear how, more generally, the different laser properties affect the interplay between competing processes and instabilities at the front surface of the target in order to ensure a robust control of electron heating and ion acceleration.

Here, we use two-dimensional (2-D) and three-dimensional (3-D) particle-in-cell (PIC) simulations with the fully relativistic electromagnetic code OSIRIS (Fonseca *et al.* 2002, 2008, 2013) to investigate in detail how the laser and plasma properties determine electron heating and how this will impact the quality of the accelerated ion beams. We focus in particular on RPA, exploring both hole boring (HB) and light sail (LS) regimes. We identify the dominant processes and establish a set of criteria relating the laser and target parameters that enable robust mitigation of electron heating and acceleration of high quality ion beams. This work presents a more detailed analysis of recently published results on the optimization of LS ion acceleration (Chou *et al.* 2022) and expands on it by presenting new results on the HB regime. The new understanding and set of conditions provided can have an important impact in the guiding of future experiments and in ensuring a better characterization of different ion acceleration regimes, by isolating the dominant mechanisms.

This paper is organized as follows. The physical regimes considered and the simulation set-up used in this study are described in § 2. In § 3, we show that suppression, or significant mitigation of electron heating is required to produce high-quality ion beams based on HB or LS. When this is not achieved, for thick targets a collisionless shock is formed which, in combination with TNSA, supersedes HB, and, for thin targets LS gives way to rapid decompression and transparency of the target. In § 4 we discuss how the deformation of the target surface due to the growth of instabilities and finite spot size effects controls electron heating. We show that the Rayleigh–Taylor-like instability (RTI) is dominant in determining the onset of strong electron heating and controlling the quality of the accelerated ion beams. Based on this understanding, we define a threshold condition for the duration of the laser pulse that allows mitigation of electron heating and

https://doi.org/10.1017/S0022377822001131 Published online by Cambridge University Press

high-quality ion acceleration in both HB and LS regimes. The effect of the laser temporal profile on ion acceleration is studied in § 5, where it is shown that the Gaussian temporal profile leads to an increase of the ion energy spread. In § 6 we discuss the importance of controlling laser prepulse to limit the electron heating due to the formation of preplasma. In § 7 we demonstrate that the new pulse duration conditions indeed minimize the electron heating and the energy spread of the accelerated ion beams over a wide range of laser and target parameters. Furthermore, we show that when the new threshold for pulse duration is combined with the condition for the optimal target thickness for LS, it limits the maximum laser intensity that can be used and the maximum peak energy of the accelerated ion beam. In § 8 we verify these findings with 3-D PIC simulations and demonstrate that based on the established criteria it is possible to generate high-quality ion beams from RPA (in both HB and LS regimes) using realistic laser and target conditions. Finally, in § 9 we present our conclusions and discuss the implications of the work for experimental studies.

2. Radiation pressure acceleration regimes and simulation set-up

We consider an intense laser interacting with a planar target with density $n_0 > n_c$ (i.e. an overdense target), where n_0 and $n_c = m_e\omega_0^2/4\pi\,\mathrm{e}^2$ are the initial plasma density and the critical density associated with laser propagation in the plasma, with e being the elementary charge, m_e the electron mass, and ω_0 the laser frequency. The intense laser exerts a coherent ponderomotive force on the electrons at the surface of the solid target, creating a charge separation between the pushed electrons and the heavier ions, which in turn accelerates the ions. In practice, the laser radiation pressure acts as a piston pushing the plasma at the front surface inwards as the laser light is reflected from the surface. Using a one-dimensional (1-D) model based on energy- and momentum-flux conservation at the target surface, one finds that the front surface is pushed at the known HB velocity (Wilks *et al.* 1992)

$$\frac{v_{\mathrm{HB}}}{c} = \sqrt{\frac{P_L}{2m_i n_i c^2}} = \sqrt{\frac{1+R}{4}\frac{Z}{A}\frac{m_e}{m_p}\frac{n_c}{n_0}}a_0\cos\theta_0, \tag{2.1}$$

where $P_L = (1+R)I\cos^2\theta_0/c$ is the radiation pressure exerted by the laser on the target surface in the normal direction, Z and A are the ion charge and mass numbers, m_i and m_p are the ion and proton masses, c the speed of light, $a_0 \simeq 0.85\sqrt{I[\mathrm{W\ cm^{-2}}](\lambda_0[\mu\mathrm{m}])^2/10^{18}}$ the peak normalized vector potential, θ_0 the incidence angle, λ_0 the wavelength of the laser and $R \leqslant 1$ the reflection coefficient. We note that R may be a function of θ_0, λ_0, a_0 and target density and composition.

We distinguish between two different RPA regimes: HB (Wilks *et al.* 1992; Macchi *et al.* 2005) and LS (Esirkepov *et al.* 2004; Robinson *et al.* 2008; Macchi & Benedetti 2010). The acceleration regime is determined by the ratio $l_0/(v_{\mathrm{HB}}\tau_0)$, where l_0 is the target thickness and τ_0 is the laser pulse duration. In the HB regime, $l_0 > v_{\mathrm{HB}}\tau_0$ and the laser radiation pressure can only push a small fraction of the target. Ions are reflected once off the laser piston acquiring a velocity $v_i \simeq 2v_{\mathrm{HB}}$, or equivalently a peak energy per nucleon $\epsilon_0 = 2m_p v_{\mathrm{HB}}^2$. In the LS regime, $l_0 < v_{\mathrm{HB}}\tau_0$ and the laser can push the whole target repeatedly during the laser pulse duration. In other words, the target is accelerated via multiple HB stages (Macchi & Benedetti 2010; Grech *et al.* 2011). In this case, the target experiences an acceleration (Macchi & Benedetti 2010)

$$a_{\mathrm{RPA}} = \frac{\mathrm{d}}{\mathrm{d}t}(v_i\gamma_i) \simeq \frac{2I}{m_i n_i l_0 c}R\frac{1-\beta_i}{1+\beta_i} \simeq 2v_{\mathrm{HB}}^2/l_0, \tag{2.2}$$

https://doi.org/10.1017/S0022377822001131 Published online by Cambridge University Press

where $\beta_i = v_i/c$ and γ_i are the normalized ion velocity and Lorentz factor. The last equality is the approximation in the non-relativistic limit. For negligible laser electron heating ($R \simeq 1$), an exact solution for the final ion velocity $\beta_{i,0}$ and the corresponding energy per nucleon ϵ_0 exists (Macchi, Veghini & Pegoraro 2009)

$$\beta_{i,0} = \frac{(1+\xi)^2 - 1}{(1+\xi)^2 + 1}; \quad \epsilon_0 = m_p c^2 \frac{\xi^2}{2(\xi+1)}, \tag{2.3a,b}$$

where $\xi = c(Zm_e n_c/Am_p n_0)(a_0^2 \tau_0/l_0)$.

In our simulations a laser pulse with frequency ω_0 is launched along the x_1 direction (which is also the direction of the target normal) from the left boundary and irradiates, unless otherwise stated, an electron–proton plasma (i.e. $m_i = m_p = 1836 m_e$) with initial density $n_0 \geqslant 40\ n_c$. A minimum density of 40 n_c corresponds to that of high-repetition rate liquid hydrogen targets (Kim, Göde & Glenzer 2016; Gauthier *et al.* 2017; Curry *et al.* 2020). The plasma density follows a step-like profile with thickness l_0. An initial electron temperature $T_e = 100$ eV is used (we have checked that our results are not sensitive to the initial temperature choice in the 10–1000 eV range). The typical size of the simulation box in 2-D (3-D) simulations is 400 (300)c/ω_0 longitudinally, and $250c/\omega_0$ transversely in x_2 (and in x_3). The 2-D (3-D) simulations use 16 (8) particles per cell per species and a spatial resolution of 0.2 (0.5)c/ω_{pe} in each direction, where $\omega_{pe} = \sqrt{4\pi\, \mathrm{e}^2 n_0/m_e}$ is the electron plasma frequency. The time step is chosen according to the Courant–Friedrichs–Lewy condition. Open (absorbing) boundary conditions for both particles and fields are used in the longitudinal and transverse directions (except in the cases with a plane wave laser where the transverse boundary conditions are periodic). We have tested different resolutions and numbers of particles per cell to ensure convergence of the results and have used a third-order particle interpolation scheme for improved numerical accuracy. We have also tested different domain sizes to ensure that this domain allows capturing the electron heating and ion acceleration dynamics without the build-up of fields at the boundaries due to the absorption of current from escaping particles. Because in most practical applications the primary interest is in highly directional ion beams, for simulations with a finite laser spot the ion energy spectra are integrated within a 10° opening angle from the laser propagation (forward) direction. We have checked that this is consistent with selecting the ions within the area of the focal spot.

To study in detail how the laser–plasma parameters affect electron heating and ion acceleration, we have performed a parameter scan in laser intensity ($a_0 = 5$–200), polarization (P-, S- and circular), incidence angle ($\theta_0 = 0°$–45°), full-width half-maximum (FWHM) duration ($\tau_0 = 30$–$2000\omega_0^{-1}$), focal spot (at $1/e^2$ beam width; $w_0 = 4$–$50c/\omega_0$ and plane wave), target composition $1 \leqslant A/Z \leqslant 4$ for single-species ions, and CH, density ($n_0 = 40$–$500n_c$, covering the range from liquid hydrogen to solid-density targets) and thickness ($l_0 = 0.08$–$40c/\omega_0$).

3. Termination of radiation pressure acceleration due to strong electron heating

In this section, we show that for thick targets (HB regime) when there is significant electron heating at the target surface, HB gives rise to the formation of a collisionless shock that is launched into the target and dominates ion acceleration. We illustrate these results with 2-D simulations where an intense ($a_0 = 12$) laser interacts with an overdense thick target ($n_0 = 42n_c$ and $l_0 = 12c/\omega_0$). The laser is either a PP (with the electric field along the x_2 direction) or CP plane wave, with a fourth-order super-Gaussian temporal profile with $\tau_0 = 100\omega_0^{-1}$.

https://doi.org/10.1017/S0022377822001131 Published online by Cambridge University Press

In figure 1(*a*,*b*), we show the longitudinal phase spaces of electrons and protons for the PP simulation near the end of the laser–plasma interaction at $t = 150\omega_0^{-1}$. We can clearly see hot electron bunches produced at a frequency of $2\omega_0$, which is a signature of the $\boldsymbol{J} \times \boldsymbol{B}$ heating mechanism (May *et al.* 2011). As a result, a significant fraction of the laser energy goes into the electron population, weakening HB. Indeed, the measured HB velocity is $v_{\mathrm{HB}} \simeq 0.026c$, consistent with a laser absorption into hot electrons of $\simeq 50\,\%$ ($R \simeq 0.5$ in (2.1)). In addition, we observe that a collisionless shock forms and dominates proton acceleration as illustrated in figure 1(*a*,*c*). The shock front detaches from the surface and propagates into the target at a nearly constant velocity $v_{\mathrm{sh}} \simeq 0.035c$. The proton population at $11c/\omega_0 \lesssim x_1 \lesssim 14c/\omega_0$ has been accelerated by the shock front to $v_i \simeq 2v_{\mathrm{sh}}$. It is important to note that even after the laser interaction finishes, the collisionless shock continues to propagate through the target and reflect protons (figure 1*c*). It is also worth noting that due to the generation of hot electrons, a strong space-charge field develops at the rear surface of the target and leads to TNSA, which is evidenced by the proton phase space at $x_1 \gtrsim 19c/\omega_0$. At later times, the protons accelerated by the shock acquire a large energy spread when they leave the target rear surface and experience TNSA. Tailoring of the rear side density profile is required to control TNSA and enable quasimonoenergetic ion beams from CSA (Fiuza *et al.* 2012, 2013). In general, we have found that in configurations in which electrons become relativistic, CSA and TNSA will dominate the ion acceleration mechanisms over HB. This highlights the need to prevent or significantly mitigate electron heating in order to enable HB to be the dominant mechanism and to produce high-quality ion beams.

A commonly employed strategy to mitigate electron heating by both $\boldsymbol{J} \times \boldsymbol{B}$ and Brunel mechanisms in laser–plasma interactions is the use of a CP laser at near normal incidence ($\theta_0 \simeq 0^\circ$; (Macchi *et al.* 2005)). The $\boldsymbol{J} \times \boldsymbol{B}$ mechanism relies on the standing wave created by the incoming and reflected laser field. For linear polarization, the oscillation of the magnetic field at the surface allows for electrons to escape the target and experience the electric field of the laser, being accelerated transversely and then rotated back into the target by the magnetic field. For circular polarization, the magnetic field of the standing wave at the target surface does not decrease to zero – it just rotates – and thus electrons cannot escape the target to be efficiently accelerated (May *et al.* 2011). The Brunel heating mechanism relies on a laser electric field component normal to the surface to directly accelerate the electrons. This is absent for normal incidence, provided that the target surface remains uniform and stable. As we will discuss in more detail in the next section, these conditions can only be maintained for very short interaction times. Figure 1(*d*–*f*) shows the results of a simulation with the same laser and plasma parameters as in figure 1(*a*–*c*) but using CP. We observe that CP is indeed capable of maintaining reduced electron heating, allowing HB to be the dominant ion acceleration mechanism. We observe that the HB velocity is $v_{\mathrm{HB}} \simeq 0.031c$, in good agreement with (2.1) for $R \simeq 1$ and that the accelerated protons have $v_1 \simeq 2v_{\mathrm{HB}}$. We also find that, in contrast to the case of a collisionless shock, the HB velocity abruptly slows down when the laser–plasma interaction ends and proton reflection/acceleration ceases (figure 1*f* at $t \simeq 165\omega_0^{-1}$). This is an interesting difference between HB and CSA that impacts the total charge accelerated by each mechanism: while HB tends to reflect a larger fraction of the background ions, it can only do so during a shorter period when compared with CSA.

In addition to the use of a CP laser at near normal incidence ($\theta_0 \simeq 0^\circ$), it has been recently proposed in the context of collisionless shock studies (Grassi *et al.* 2017) that S-polarization (SP) (with the electric field along the x_3 direction) with a large incidence angle can also achieve similar results in terms of mitigating electron heating. This is because Brunel heating is absent for SP and $\boldsymbol{J} \times \boldsymbol{B}$ heating can be significantly reduced

https://doi.org/10.1017/S0022377822001131 Published online by Cambridge University Press

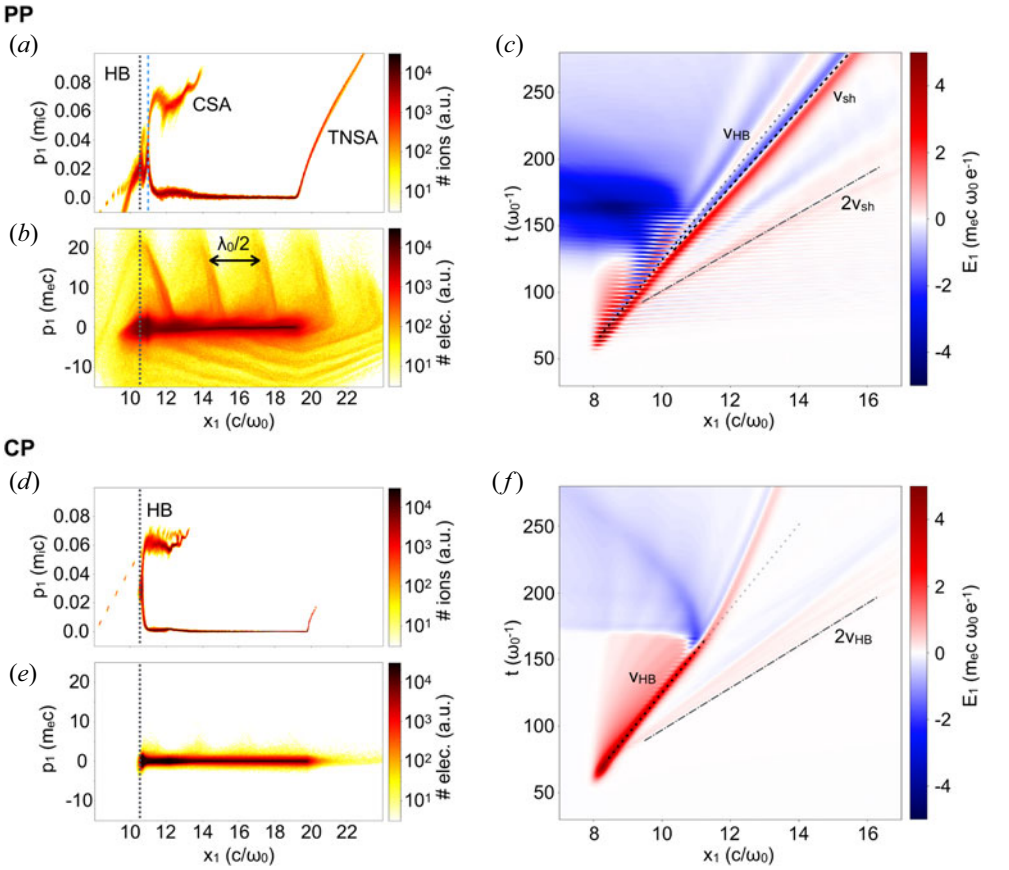

FIGURE 1. Results of 2-D PIC simulations of a P-polarized (PP) (*a–c*) and circularly polarized (CP) (*d–f*) short-pulse laser ($a_0 = 12$) interacting with an overdense target ($n_0 = 42n_c$). Longitudinal $p_1 - x_1$ phase spaces, shown at $t = 150\omega_0^{-1}$, of protons (*a*,*d*), electrons (*b*,*e*) and time evolution of the longitudinal E_1 electric field (*c*,*f*). The laser pulse irradiates the target from the left-hand side, has a super-Gaussian temporal profile, and ends at $t \simeq 160\omega_0^{-1}$. For a PP laser, the electrons are heated by the laser, HB is weakened, and a collisionless shock develops, which dominates the proton acceleration. The electrostatic shock front detaches from the HB front and propagates at $v_{\rm sh} \simeq 0.035c$, which reflects the protons to a speed of $2v_{\rm sh}$. The electrons in the CP case remain relatively cold and HB is the dominant ion acceleration mechanism, accelerating protons to $2v_{\rm HB}$, where $v_{\rm HB} \simeq 0.031c$. After the laser ends, the HB front decays and slows down. In the phase spaces, the dotted lines denote the target front surface (with density $n \simeq n_c$) and the dashed blue line indicates the collisionless shock front. In (*c*) and (*f*), the dotted, dashed and dash–dotted lines indicate $v_{\rm HB}$, $v_{\rm sh}$ and the proton beam velocity ($2v_{\rm HB}$ or $2v_{\rm sh}$), respectively.

since it scales with $\cos\theta_0$. We have explored this possibility over a large range of laser intensities ($a_0 = 5$–30) and plasma densities ($n_0 = 40$–$150n_c$) and confirmed that in 2-D simulations indeed SP with $\theta_0 = 45^\circ$ can significantly suppress electron heating and lead to HB ion acceleration comparable to the CP case (not shown here). However, the situation changes significantly for more realistic 3-D simulations. In 3-D simulations, the laser–plasma interaction along the direction of laser polarization is effectively PP at $\theta_0 \simeq 0^\circ$ and gives rise to significant electron heating along the laser polarization. In all 3-D SP cases tested, hot electrons acquire relativistic temperature and we observe a transition from HB to CSA similar to the PP case illustrated in figure 1(*a–f*).

https://doi.org/10.1017/S0022377822001131 Published online by Cambridge University Press

For very thin targets, corresponding to the LS regime, we have observed similar results in terms of the mitigation of electron heating, which was achieved with a CP laser with $\theta_0 \simeq 0^\circ$ and led to the acceleration of ions with a narrow energy spread. We note that for PP and SP, the onset of strong electron heating does not lead to the formation of a collisionless shock. Instead, we observe that the thin target quickly becomes transparent to the laser and the radiation pressure is no longer efficient in accelerating ions. Overall, for both HB and LS regimes, we find that the use of CP is required to significantly mitigate electron heating and optimize RPA. Non-normal incidence angles can be useful for SP, but unfortunately seem to be only effective in 2-D simulations. In the remainder of this paper, we discuss in detail the impact of the laser and plasma parameters on electron heating with CP for both HB and LS regimes in order to understand the set of conditions required for high-quality ion acceleration.

4. Development of surface corrugations

The interaction of an intense laser with an overdense target can significantly modify the shape of the target surface either due to the development of surface instabilities or from finite laser spot size effects. These modulate the surface density profile, which can ultimately trigger strong electron heating (e.g. Klimo *et al.* 2008; Dollar *et al.* 2012; Paradkar & Krishnagopal 2016), even for a CP laser, and impact the quality and mechanisms of ion acceleration as discussed above. In this section, we discuss the importance of surface corrugations on HB and LS acceleration regimes with a CP laser.

4.1. *Growth of surface instabilities*

Previous studies have investigated the development of density ripples at the interaction surface and there has been significant discussion on which instabilities are dominant, including the Weibel instability (Sentoku *et al.* 2000), RTI (Gamaly 1993; Pegoraro & Bulanov 2007; Palmer *et al.* 2012; Khudik *et al.* 2014; Eliasson 2015; Sgattoni *et al.* 2015), electron–ion coupling instabilities (Wan *et al.* 2016; Wan *et al.* 2018) or a combination of these (Wan *et al.* 2020). However, the correlation between these instabilities and the onset of electron heating has not been studied systematically for both HB and LS. Here, we begin by illustrating the surface dynamics and electron heating for the interaction of a CP laser with Gaussian longitudinal and transverse intensity profiles with a target at normal incidence using 2-D PIC simulations. In the HB regime, we use a laser with $a_0 = 27$, $\tau_0 = 200\omega_0^{-1}$, $w_0 = 50c/\omega_0$ with $n_0 = 40\,n_c$ and $l_0 = 75c/\omega_0$; for LS, $a_0 = 15$, $\tau_0 = 105\omega_0^{-1}$, $w_0 = 50c/\omega_0$, with $n_0 = 250\,n_c$ and $l_0 = 0.085c/\omega_0$ are used. The results are shown in figure 2(*a*) for HB and figure 3(*a*) for LS, respectively.

We observe that indeed, even with CP, there is the onset of strong electron heating after a relatively short interaction time. In the HB regime (figure 2*a*), the electron and ion phase spaces at $t = 150\omega_0^{-1}$ show that electrons have been heated to relativistic temperatures, which leads to a significant weakening of the laser radiation pressure and to the formation of a collisionless shock and development of strong TNSA field that dominate ion acceleration, similarly to what was observed for the PP case discussed in § 3. A sharp increase of the FWHM energy spread of the accelerated ions ensues, reaching $\Delta\epsilon/\epsilon_0 > 100\,\%$ as can be seen in figure 2(*c*); and by $t = 225\omega_0^{-1}$ both the electron temperature and ion energy spread have saturated at large values.

In the LS regime (figure 3*a*), we observe that once the electrons are significantly heated they drive the rapid expansion of the target and broadening of the ion energy spread (figure 3*c*) due to the associated strong space-charge field and short target thickness. By $t = 115\omega_0^{-1}$ the target expansion leads to the onset of relativistic transparency as can be

https://doi.org/10.1017/S0022377822001131 Published online by Cambridge University Press

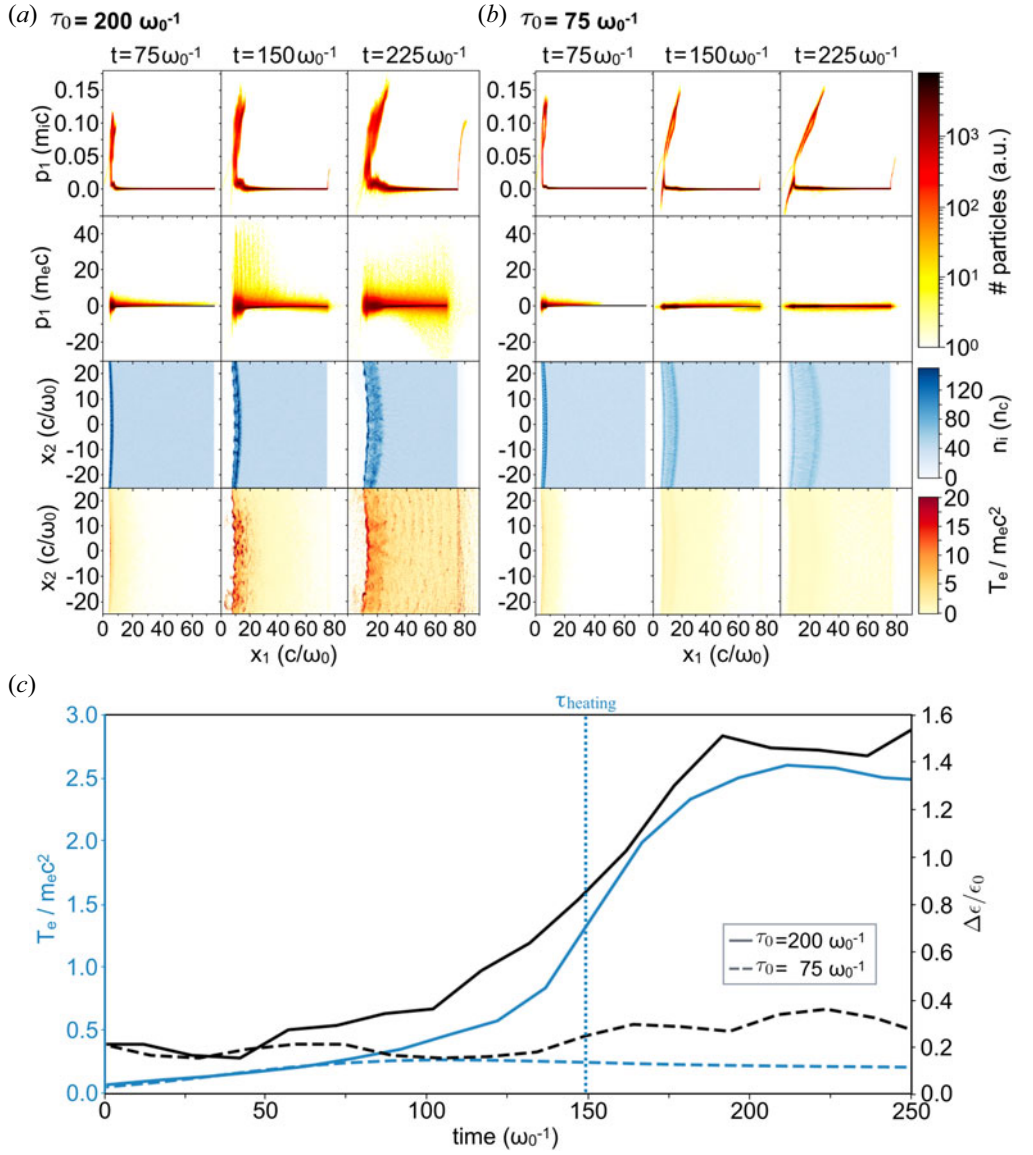

FIGURE 2. Results of 2-D PIC simulations of the interaction of an intense Gaussian CP laser pulse with an overdense target in HB regime. (*a*,*b*) Longitudinal $p_1 - x_1$ ion (top row) and electron (second row) phase spaces, ion density profile (third row) and local electron temperature (bottom row). The laser pulse durations are $\tau_0 = 200$ and $75\omega_0^{-1}$ in (*a*) and (*b*), respectively. (*c*) Temporal evolution of T_e (blue, left-hand axis) and ion beam energy spread $\Delta\epsilon/\epsilon_0$ (black, right-hand axis). The time $t = 0$ is defined as $\tau_0/2$ before the laser peak intensity reaches the target.

seen in figure 3(*c*) from the evolution of $n_e/(\gamma n_c)$ (the ratio of the electron density, n_e, and relativistic critical density at the target front surface, where γ is the average Lorentz factor of the electrons). At this point, RPA is terminated and the ion energy distribution ceases to be peaked.

https://doi.org/10.1017/S0022377822001131 Published online by Cambridge University Press

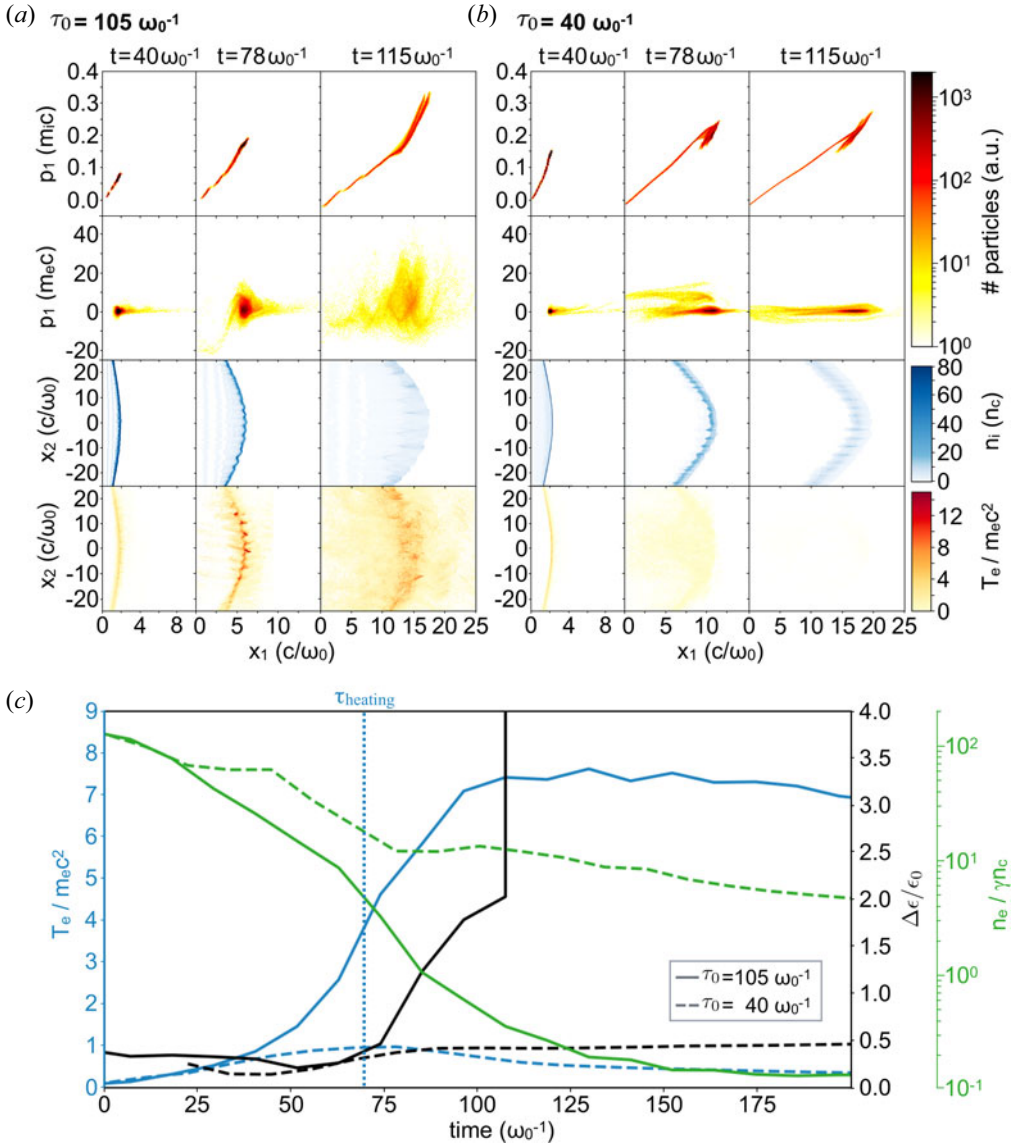

FIGURE 3. Same as figure 2 but for LS, where the laser pulse durations are $\tau_0 = 105$ and $40\omega_0^{-1}$ in (*a*) and (*b*), respectively. In (*c*) the green, rightmost axis plots $n_e/(\gamma n_c)$.

From the temporal evolution of the electron temperature T_e (average kinetic energy of electrons) and FWHM ion energy spread $\Delta\epsilon/\epsilon_0$ shown in figures 2(*c*) and 3(*c*) for the HB and LS regimes, respectively, we observe that they follow a similar behaviour with the ion beam energy spread increasing sharply following the rapid growth of T_e in both cases. We define this time associated with the onset of strong electron heating, τ_{heating}, as the time for which the rate of increase of the electron temperature, $\mathrm{d}T_e/\mathrm{d}t$, is maximum.

We have repeated the same simulations in both regimes but using a shorter laser pulse with $\tau_0 = 75\omega_0^{-1}$ and $\tau_0 = 40\omega_0^{-1}$, both $< \tau_{\text{heating}}$, for HB and LS, respectively, to confirm the impact of electron heating on the growth of the ion energy spread and overall target dynamics. The results are shown in figures 2(*b*,*c*) and 3(*b*,*c*). In these cases, we observe

https://doi.org/10.1017/S0022377822001131 Published online by Cambridge University Press

that indeed both T_e and $\Delta\epsilon/\epsilon_0$ remain low (figures 2c and 3c). The ion beam energy spread saturates at $t \simeq 2\tau_0$ with $\Delta\epsilon/\epsilon_0 \ll 1$ and remains stable long after the laser–plasma interaction has finished.

We have found that the onset of electron heating in both HB and LS regimes is related to the emergence of large transverse density modulations at the target front surface with a wavelength comparable to that of the laser. For the longer pulse simulations ($\tau_0 > \tau_{\text{heating}}$), these surface density modulations are visible in the third rows of figures 2(*a*) and 3(*a*) at the times where electron heating is also observed. Density modulations with a wavelength comparable to λ_0 allow the penetration of the laser in the lower density regions and resonant enhancement of its electric field (Eliasson 2015; Sgattoni *et al.* 2015), giving rise to effective electron heating, for example via the Brunel mechanism (bottom rows of figures 2*a* and 3*a*), with the temperature reached being comparable to that observed in simulations with a linearly polarized laser (not shown here). The spatial distribution of T_e shows indeed that the heating is happening at the walls of these concave valleys and consistent with direct acceleration by the laser electric field. The location of the hot spots of T_e oscillates (from top to bottom of the valleys) in accordance with the phase of the laser electric field. In the simulations with $\tau_0 < \tau_{\text{heating}}$, the amplitudes of the density modulations at the surface are much smaller during the time of laser interaction (third rows of figures 2*b* and 3*b*) leading to a much-reduced electron heating and stable ion acceleration.

In order to study the mechanism responsible for these corrugations, and isolate the effects of surface instabilities, we have performed a parameter scan of 2-D simulations with a long, plane-wave CP laser at normal incidence, with parameters varied in the following ranges: for HB, $5 \leqslant a_0 \leqslant 60, 40n_c \leqslant n_0 \leqslant 200n_c$; for LS, $5 \leqslant a_0 \leqslant 200, 40n_c \leqslant n_0 \leqslant 500n_c$ and $0.08c/\omega_0 \leqslant l_0 \leqslant 2c/\omega_0$. Note that for the LS regime, the initial target thickness l_0 is always larger than or equal to the optimal LS target thickness l_{opt}, defined as $l_{\text{opt}} = a_0\lambda_0 n_c/(\sqrt{2}\pi n_0)$, for which the acceleration is maximized by minimizing the total target mass while guaranteeing that the target remains relativistically opaque (Macchi *et al.* 2009). For both regimes, the target is either composed of single-species ions with $1 \leqslant A/Z \leqslant 4$, or CH (plastic). We analyse the growth of ion density modulations by computing the transverse Fourier modes (k_{x_2}) of the longitudinal (x_1) displacement of the relativistic critical surface ($n \simeq \gamma_0 n_c$; where $\gamma_0 = \sqrt{1 + a_0^2/2}$ is the electron Lorentz factor), as a function of the transverse (x_2) position (e.g. figure 4*b*,*e*). Previous theoretical studies of surface instabilities considered perturbations of the surface displacement and showed it will grow exponentially due to instability (e.g. Gamaly 1993; Eliasson 2015). Alternatively, for LS, one could obtain the Fourier modes of the amplitude of the transverse density profile by integrating over the target longitudinally. We have checked that the obtained growth rates and time scales of the different modes are consistent between both methods.

Figure 4 illustrates the growth of different modes for simulations with the same laser intensity and target parameters of figures 2 and 3. Note that both targets remain opaque to the laser during the time of the analysis and thus the measurements of the growth rates and saturation levels are not affected by the onset of relativistic transparency. The fastest growing modes are observed at $k_{x_2} \gg k_0$, with $k_0 = 2\pi/\lambda_0$ (e.g. $k_{x_2} \simeq 13\omega_0/c$ in figure 4*e* at $t \simeq 30\omega_0^{-1}$), and have been previously described as associated with electron–ion coupling instabilities (Wan *et al.* 2016; Wan *et al.* 2018, 2020). However, these modes saturate at relatively low amplitude and do not lead to significant electron heating. The dominant density modulations are associated with the mode with $k_{x_2} \simeq k_0$ and we observe the onset of strong electron heating during the linear growth and saturation of this mode.

https://doi.org/10.1017/S0022377822001131 Published online by Cambridge University Press

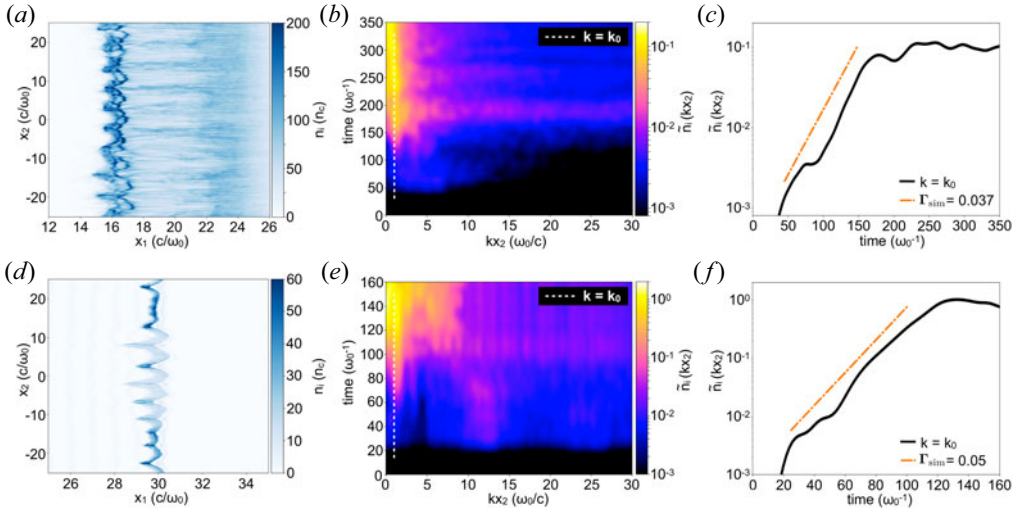

FIGURE 4. Development of surface corrugations in HB (*a–c*) and LS (*d–f*) regimes. (*a*,*d*) Proton density showing transverse density corrugations near the interaction surface at $t = 200\omega_0^{-1}$ for (*a*) and $t = 90\omega_0^{-1}$ for (*d*). (*b*,*e*) Evolution of Fourier modes at the relativistic critical surface of the corrugation amplitudes $\tilde{n}_i(k_{x_2})$. The dashed white line denotes the $k_{x_2} = k_0$ mode. (*c*,*f*) Time evolution of the $k_{x_2} = k_0$ mode and its linear fit.

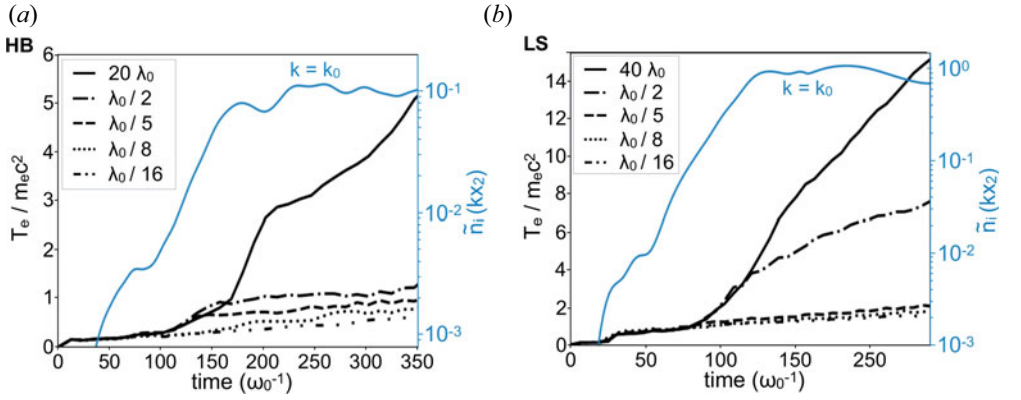

FIGURE 5. Evolution of electron temperature for different transverse simulation domain sizes (black, left-hand axis). The solid black curves correspond to the simulations in figure 4 with a transverse box size of $20\,\lambda_0$ for HB (*a*) and $40\,\lambda_0$ for LS (*b*), respectively. For these cases the growths of the $k_{x_2} = k_0$ (solid) mode are shown (blue, right-hand axis).

This suggests that the onset of strong electron heating is related to laser-driven RTI for which the dominant mode is $k_{x_2} \simeq k_0$ (Eliasson 2015; Sgattoni *et al.* 2015).

To further confirm that the RTI mode with $k_{x_2} = k_0$ is the dominant effect on the onset of strong electron heating and degradation of the ion beam quality, we have performed additional simulations with different transverse domains. We observe that for transverse domain sizes $< \lambda_0/2$, where the dominant RTI mode is prohibited, no significant electron heating is observed. In these cases, the fastest growing high-k modes are still captured and thus can still grow, but T_e remains very low (figure 5). For the largest transverse domain size $\gg \lambda_0$, we see that strong electron heating starts near the saturation time of the RTI.

https://doi.org/10.1017/S0022377822001131 Published online by Cambridge University Press

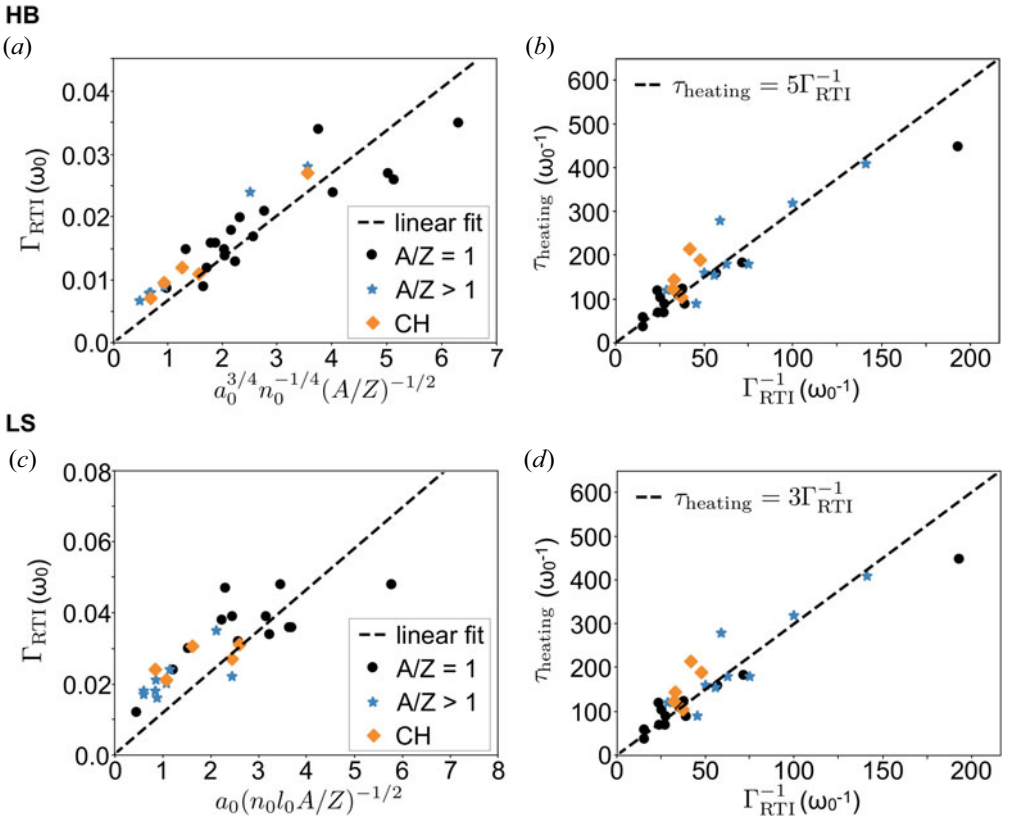

FIGURE 6. Scaling of the measured growth rate of the $k_{x_2} = k_0$ mode of the surface corrugations (*a*,*c*), and strong correlation between the electron heating time $\tau_{\rm heating}$ and the growth time of the RTI (*b*,*d*), for both HB (*a*,*b*) and LS (*c*,*d*). Coloured symbols are measurements from 2-D PIC simulations.

For the laser-driven RTI, the growth rate is $\Gamma_{\rm RTI} \propto \sqrt{a_{\rm RPA} k_0}$, where $a_{\rm RPA} = 2v_{\rm HB}^2/l$ is the acceleration due to radiation pressure ((2.2) with $R \simeq 1$ and $\beta_i \ll 1$). For LS, the target thickness is l_0, whereas for HB the effective acceleration layer is characterized by the relativistic electron skin depth $l = \sqrt{a_0} c/\omega_{pe}$ (Gamaly 1993). Linear fits to the measured growth rates of the k_0 mode from the simulations confirm the expected scaling with the following numerical factors (figure 6; see also the example fits in figure 4*c*,*f*): $\Gamma_{\rm RTI}[\omega_0] \simeq 0.3 a_0^{3/4} (n_0[n_c])^{-1/4} (Zm_e/(Am_p))^{1/2}$ for HB and $\Gamma_{\rm RTI}[\omega_0] \simeq 0.5 a_0 (n_0[n_c] l_0[c/\omega_0] Am_p/(Zm_e))^{-1/2}$ for LS.

We find a strong correlation between $\tau_{\rm heating}$ and the growth time of the instability, with $\hat{\tau}_{0,\rm RTI} \equiv \tau_{\rm heating} \simeq 5\Gamma_{\rm RTI}^{-1}$ for HB and $\hat{\tau}_{0,\rm RTI} \equiv \tau_{\rm heating} \simeq 3\Gamma_{\rm RTI}^{-1}$ for LS, where $\hat{\tau}_{0,\rm RTI}$ is defined as the time of the onset of strong electron heating due to the development of the RTI. This is shown in figures 6(*b*) and 6(*d*). In order to suppress or significantly mitigate electron heating, the duration of the laser pulse τ_0 should then be smaller than $\hat{\tau}_{0,\rm RTI}$, which can be written as

$$\hat{\tau}_{0,\rm RTI}[\rm fs] \simeq \begin{cases} 400 a_0^{-3/4} \lambda_0[\mu\rm m] \left(\dfrac{n_0}{n_c}\right)^{1/4} \left(\dfrac{A}{Z}\right)^{1/2} & \text{for HB,} \\ 350 a_0^{-1} \left(l_0[\mu\rm m] \lambda_0[\mu\rm m] \dfrac{A}{Z} \dfrac{n_0}{n_c} \right)^{1/2} & \text{for LS.} \end{cases} \tag{4.1}$$

https://doi.org/10.1017/S0022377822001131 Published online by Cambridge University Press

It is important to note that although several previous works have studied the development of the RTI, the focus had been on developing strategies to mitigate the penetration of the RTI fingers on the accelerated proton species, which included the use of mixed ion species (Yu *et al.* 2010, 2011), advanced laser configurations (Wu *et al.* 2014; Zhou *et al.* 2016) and curved targets (Wang, Khudik & Shvets 2021). These are either challenging to implement in practice (Zhou *et al.* 2016; Wang *et al.* 2021; and have not yet been proven to be effective experimentally), or still lead to significant electron heating (Yu *et al.* 2010; Wu *et al.* 2014). As we show here, a quantitative understanding of the detrimental effect that the instability-induced electron heating has on the ion beam quality is critical to produce ion beams with high spectral quality.

We should further note that the results presented here have considered only the regime where ions are non-relativistic, which is appropriate for most current and near-future laser systems. In the relativistic regime, the RTI can still grow as shown in previous numerical studies (Bulanov *et al.* 2010; Sgattoni, Sinigardi & Macchi 2014), but how its growth rate changes and, more generally, its impact on electron heating and the spectral quality of the accelerated ions is not well established. One expects that strong electron heating will still be caused by the development of RTI in the relativistic regime – Brunel heating will still be present. The resulting space-charge fields will also lead to an increase of the ion energy spread, however, the rate at which this happens may be more moderate in the relativistic regime when compared with the non-relativistic case. Furthermore, the resulting expansion of the target will also pose limitations on the acceleration due to the onset of relativistic transparency, as in the cases discussed here. A detailed analysis of the relativistic regime is left for future work.

4.2. *Finite laser spot size*

The transverse variation of the laser intensity due to its spatial profile naturally leads to non-uniform HB velocities across the surface and results in a change of the surface shape over time, also triggering strong electron heating. The onset time of strong electron heating is approximately when the radiation-pressure-driven displacement d of the target surface is comparable to the laser spot size w_0, resulting in a significant change in the local incidence angle. This effect has been previously discussed in the case of normal laser incidence ($\theta_0 = 0^\circ$ (Klimo *et al.* 2008; Wan *et al.* 2020)). In fact, this argument can be generalized to other laser incidence angles if we consider the displacement d to be along the axis of the laser resulting in a time for electron heating that is independent of θ_0. We define this time as $\hat{\tau}_{0,\mathrm{FS}}$ ('FS' stands for finite spot), and can estimate it as $d(\hat{\tau}_{0,\mathrm{FS}}) = w_0$, where for simplicity we assume that the laser intensity is approximately constant in time. For HB, we have $d(t) = v_{\mathrm{HB}}t$. For LS, we consider first that the target experiences a constant acceleration in its rest frame – i.e. $a_{\mathrm{RPA}} \simeq 2v_{\mathrm{HB}}^2/l_0$ ((2.2) with $R \simeq 1$ and $\beta_i \ll 1$). This then gives $d(t) = (c\sqrt{c^2 + a_{\mathrm{RPA}}^2 t^2} - c^2)/a_{\mathrm{RPA}} \simeq (cl_0/2v_{\mathrm{HB}}^2)(\sqrt{c^2 + 4v_{\mathrm{HB}}^4 t^2/l_0^2} - c)$ (for all cases considered, we have found that the error introduced by taking the non-relativistic ion velocity limit is $\lesssim 5\,\%$). Equating $d(\hat{\tau}_{0,\mathrm{FS}}) = w_0$ yields

$$\hat{\tau}_{0,\mathrm{FS}}[\mathrm{fs}] \simeq \begin{cases} 200a_0^{-1} w_0[\mu\mathrm{m}] \left(\dfrac{An_0}{Zn_c}\right)^{1/2} & \text{for HB,} \\ 200a_0^{-1} \left(\dfrac{w_0[\mu\mathrm{m}] l_0[\mu\mathrm{m}] An_0}{Zn_c}\right)^{1/2} & \text{for LS.} \end{cases} \tag{4.2}$$

We note that the estimate above considers near diffraction-limited laser focusing where the transverse intensity profile is smooth. If the Strehl ratio is low and speckle-like intensity distributions are present at focus, these will lead to modulations of the surface and laser

https://doi.org/10.1017/S0022377822001131 Published online by Cambridge University Press

incidence angle on scales comparable to the speckle size. In that case, in the threshold condition given in (4.2) we should replace w_0 by the size of the laser intensity speckles, which can be a significant limitation for small-scale ($\sim\lambda_0$) speckles. We further note that with oblique incidence ($\theta_0 > 0$), the ion beam direction will be modified. This can happen due to partial absorption of the laser field, which will impart transverse (along the target surface) momentum to the ions (Macchi *et al.* 2019) and also as the surface is modified to be nearly normal to the laser pulse causing the ion beam direction to be primarily along the laser propagation direction.

4.3. *Dominance of the RTI*

We now compare the constraints on τ_0 imposed by the RTI via (4.1) and the finite spot size effect via (4.2). Rayleigh–Taylor-like instability dominates when $\hat{\tau}_{0,\mathrm{RTI}} < \hat{\tau}_{0,\mathrm{FS}}$, or equivalently $w_0/\lambda_0 \gtrsim 2[a_0 n_c/n_0]^{1/4}$ for HB, and $w_0/\lambda_0 \gtrsim 3$ for LS. These conditions are met for targets that are relativistically opaque ($a_0 < n_0/n_c$) and for typically used spot sizes $w_0 \gtrsim$ (2–3) λ_0 (assuming near diffraction-limited laser intensity profiles at focus). Thus, we expect that for conditions of interest for laser-driven ion acceleration in overdense targets the surface corrugations by RTI discussed here impose the main limitation on the pulse duration, (4.1), for high-quality ion beam acceleration.

5. Laser temporal profile

In this section, we evaluate how different laser temporal profiles impact the quality of the ion beam. This can be particularly relevant for the HB regime, as different ion populations will experience different HB velocities due to $v_{\mathrm{HB}}(t) \propto a_0(t)$. We have performed simulations in both HB and LS regimes, for a plane wave laser with $\tau_0 < \hat{\tau}_{0,\mathrm{RTI}}$, where the laser temporal profile is either Gaussian or a flat-top (approximated by a fourth-order super-Gaussian). The total laser energy and a_0 is kept the same in both cases. The range of a_0, n_0 and l_0 explored was similar to § 4, and we have varied the pulse duration in the range $0.2\hat{\tau}_{0,\mathrm{RTI}} \lesssim \tau_0 < \hat{\tau}_{0,\mathrm{RTI}}$.

In general, we find that the accelerated proton beams have a relatively narrow energy spread with both profiles, but the energy spread in the Gaussian case is typically larger, by a factor up to $\simeq 2$. Figure 7 illustrates the typical differences between both profiles for HB and LS. One important feature that we observe in the HB regime is the development of an extended low-energy population (<3 MeV in figure 7*a*). This is due to the contribution from the low HB velocity phase at the edges of the laser pulse, and can be understood as follows. In a time interval t to $t + \mathrm{d}t$, a population of ions $\mathrm{d}N \propto n_i v_{\mathrm{HB}}(t)\,\mathrm{d}t$ is accelerated to a velocity $2v_{\mathrm{HB}}(t) \propto a_0(t)$ (for $R \simeq 1$). Therefore, the resulting energy spectrum will be

$$\frac{\mathrm{d}N}{\mathrm{d}\epsilon} = \frac{\mathrm{d}N}{\mathrm{d}t}\frac{\mathrm{d}t}{\mathrm{d}\epsilon} \propto \frac{1}{\sqrt{\epsilon \ln(\tilde{\epsilon}_0/\epsilon)}}, \tag{5.1}$$

for a Gaussian pulse, where $\tilde{\epsilon}_0 = 2m_i v_{\mathrm{HB},0}^2$ is the peak energy of the ions (with $v_{\mathrm{HB},0}$ the HB velocity associated with the peak intensity). This matches well the low-energy component of the proton spectrum in figure 7(*a*), which is responsible for the additional energy spread with respect to the flat-top case.

6. Laser prepulse

In this section, we explore the impact that the development of a preplasma induced by a laser prepulse can have in triggering early electron heating and affecting the spectral quality of ion beams accelerated via RPA. We consider a preplasma with an exponential density profile at the front surface of the target with scale length l_g. For the laser and target

https://doi.org/10.1017/S0022377822001131 Published online by Cambridge University Press

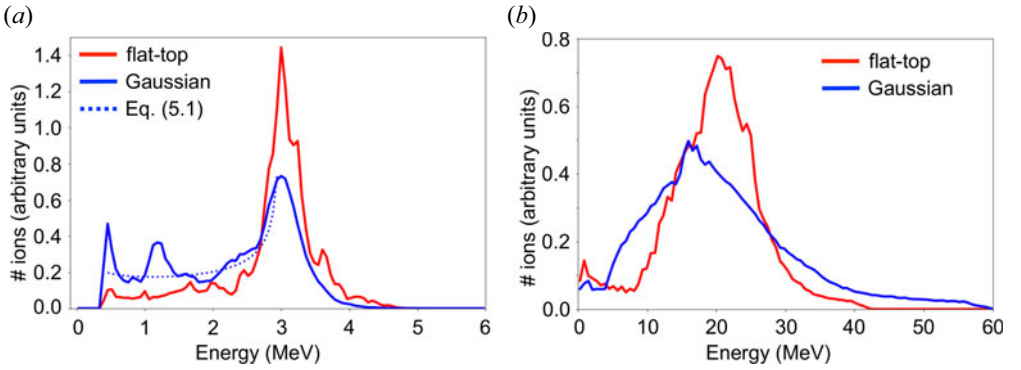

FIGURE 7. Proton energy spectra from 2-D PIC simulations of plane-wave CP laser pulses ($a_0 = 30$) with either Gaussian (blue) and flat-top (red) temporal profiles normally incident on a target ($n_0 = 136n_c$), plotted at the time the laser ends, for (*a*) HB (with a semi-infinite target) and (*b*) LS ($l_0 = 0.5c/\omega_0$). The Gaussian pulse has $\tau_0 = 40\omega_0^{-1}$ and the flat-top profile is approximated by a fourth-order super-Gaussian temporal profile, where the total laser energy is kept the same as the Gaussian pulse. The dotted curve in (*a*) describes the low-energy component of the spectrum (see (5.1)).

parameters considered in the short-pulse cases in figure 2(*b*) and 3(*b*), with $\tau_0 = 75\omega_0^{-1}$ and $l_0 = 75c/\omega_0$ for HB and $\tau_0 = 40\omega_0^{-1}$ and $l_0 = 0.085c/\omega_0$ for LS, we have performed additional simulations with different levels of l_g, which was varied in the range $0.01 \leqslant l_g/l_0 \leqslant 0.4$ (the total target mass is conserved).

Figure 8 shows that the preplasma can significantly impact electron heating and the ion energy spread for levels of $l_g \gtrsim 0.1\, l_0$. In the case of HB, the electron temperature and ion energy spread for a preplasma scale length $l_g < 0.1l_0$ ($l_g < 1.2$ μm for $\lambda_0 = 1$ μm) are similar to the case of no preplasma, but above this level strong electron heating is triggered, leading to a very fast degradation of ion beam quality even before the pulse arrives at the main target. For LS, for a preplasma with $l_g \leq 0.1l_0$ the results are also very similar to the no preplasma case. However, for $l_g \gtrsim 0.2l_0$ ($l_g \gtrsim 2.7$ nm for $\lambda_0 = 1$ μm) both the electron temperature and ion energy spread are observed to increase to nearly twice the values of the no preplasma case. These results confirm the need to carefully control the level of preplasma to produce ion beams with high spectral quality from RPA and will help inform the laser prepulse contrast requirements for future experimental studies.

7. Optimal regime of radiation pressure acceleration

Our findings make clear the importance of limiting the pulse duration to control electron heating and obtain quasimonoenergetic ion beams from RPA in both HB and LS regimes. In figure 9 we demonstrate that (4.1) is robust over a wide range of laser and target parameters even when realistic Gaussian transverse and temporal pulse profiles are considered. We observe that, indeed, the derived threshold condition marks the transition from low to high electron heating (figure 9*a*,*c*) and consequently from low to high energy spread of the accelerated ion beam (figure 9*b*,*d*). By repeating some of the simulations in the high-quality regimes using a small, but finite laser incidence angle, we have also confirmed that in general for an incidence angle $\lesssim 10^\circ$, as typically used experimentally, electron heating is still maintained at a low level and the quality of the ion beam remains similar to the case with normal incidence.

https://doi.org/10.1017/S0022377822001131 Published online by Cambridge University Press

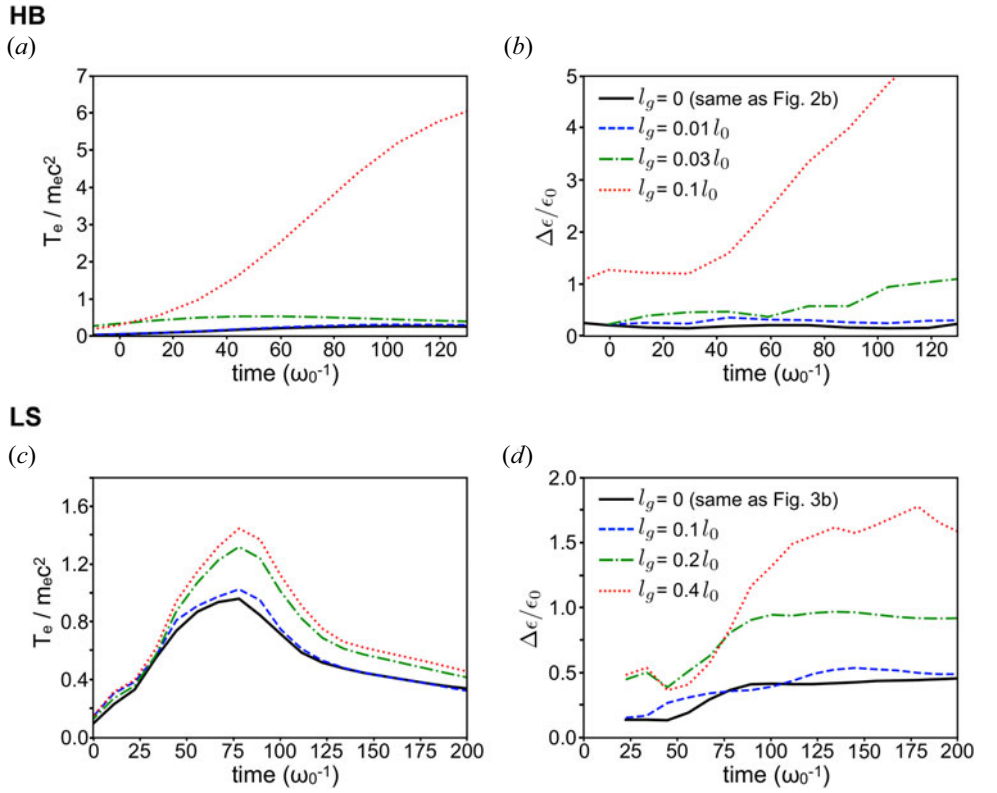

FIGURE 8. Results of 2-D PIC simulations of the interaction of an intense Gaussian CP laser pulse with a planar target of thickness l_0 and an exponential preplasma of scale length l_g in the front, in both HB (*a*,*b*) and LS (*c*,*d*) regimes. (*a*,*c*) Temporal evolution of electron temperature T_e and (*b*,*d*) ion beam energy spread $\Delta\epsilon/\epsilon_0$. Here $\Delta\epsilon/\epsilon_0$ is measured for protons within a 10° opening angle with respect to the laser propagation direction (target normal) and the time $t = 0$ is defined as $\tau_0/2$ before the laser peak intensity reaches the main target.

For the LS regime, combining the threshold condition for the pulse duration (see (4.1)) and the optimal target thickness condition $l_0 = l_{\rm opt}$ results in a new condition on the maximum laser intensity with important implications for the optimization of ion beam energy spread in LS acceleration (Chou *et al.* 2022). In particular, we obtain that the laser a_0 should be limited by

$$a_0 \lesssim \hat{a}_0 \equiv \frac{350^2}{\sqrt{2}\pi}\frac{A}{Z}\left(\frac{\lambda_0[\mu\mathrm{m}]}{\tau_0[\mathrm{fs}]}\right)^2, \tag{7.1}$$

and consequently the maximum energy per nucleon ϵ_0 of the narrow energy spread peak is

$$\hat{\epsilon}_0 = m_p c^2 \frac{\hat{\xi}^2}{2(\hat{\xi}+1)}, \quad \text{where } \hat{\xi} \simeq 20\frac{\lambda_0[\mu\mathrm{m}]}{\tau_0[\mathrm{fs}]}. \tag{7.2}$$

In contrast to previous works, and to the common practice of pushing for higher a_0 to generate stable LS and higher energy ion beams (e.g. Qiao *et al.* 2009), (7.1) and (7.2) indicate the existence of a maximum $\hat{a}_0$ and $\hat{\epsilon}_0$ for high-quality LS ion beams, and show that these are determined primarily by the laser wavelength and pulse duration. In

https://doi.org/10.1017/S0022377822001131 Published online by Cambridge University Press

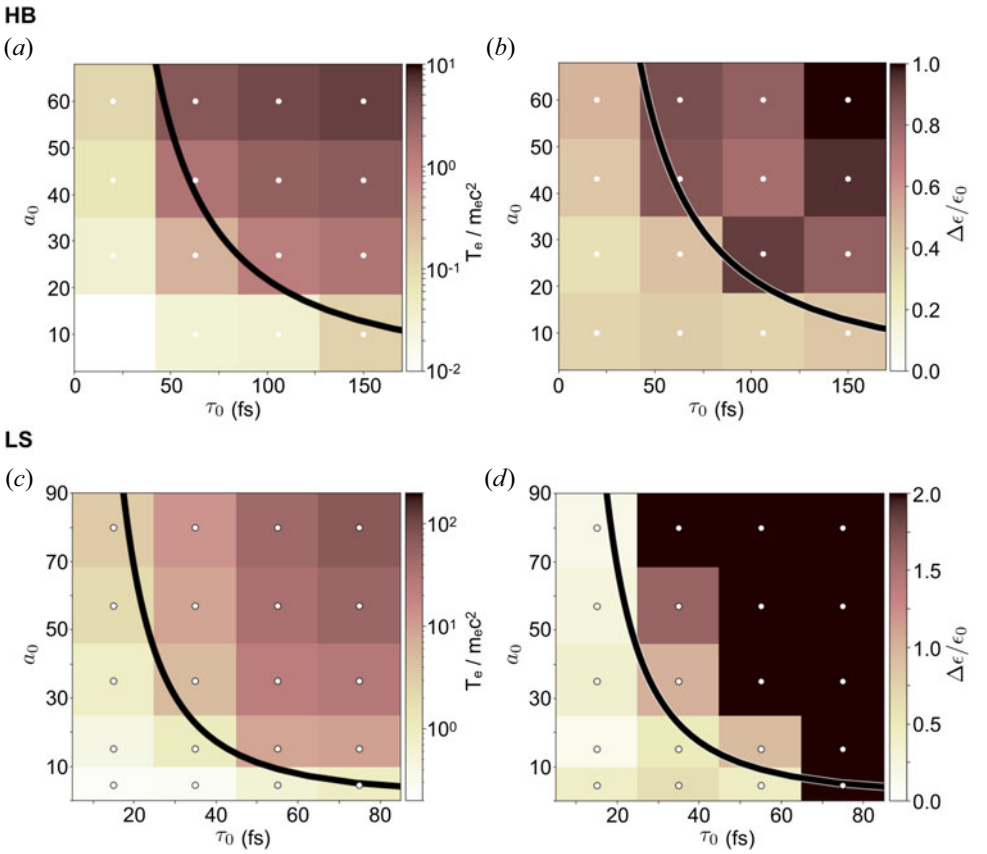

FIGURE 9. (*a*,*c*) Electron temperature T_e and (*b*,*d*) ion beam energy spread $\Delta\epsilon/\epsilon_0$ measured from 2-D PIC simulations of a 1 μm wavelength Gaussian laser pulse with duration τ_0 and spot size $w_0 = 7.6$ μm interacting with a solid target with $n_0 = 40\,n_c$, $l_0 = 12$ μm for HB (top row) and $250n_c$, $l_0 = l_{\rm opt}$ for LS (bottom row). Here T_e is measured at the end of the laser interaction when the maximum is observed. Here $\Delta\epsilon/\epsilon_0$ is measured for protons within a 10° opening angle at $t \simeq 2\tau_0$. The black curves correspond to the prediction of (4.1) and the white dots denote the parameters sampled by the simulations.

particular, it is worth highlighting that for this optimal regime of acceleration the energy per nucleon of the ion spectral peak does not depend on the target density, composition and laser energy (transverse spot size). These predictions for the LS regime have been recently validated with 3-D simulations in Chou *et al.* (2022).

8. The 3-D simulation results

To further explore RPA in more realistic 3-D configurations and validate our model for the optimal laser duration for high-quality ion beams, we have performed 3-D simulations in both HB and LS regimes.

In the HB regime, a CP laser with $a_0 = 12$ ($I \simeq 2 \times 10^{20}$W cm^{-2} for $\lambda_0 = 1$ μm), $w_0 = 2$ μm is incident with $\theta_0 = 0°$ on a planar electron–proton target with $n_0 = 40n_c$ and thickness of 3.5 μm, corresponding to the conditions of typical liquid hydrogen jet targets (Kim, Göde & Glenzer 2016; Gauthier *et al.* 2017; Göde *et al.* 2017; Obst *et al.* 2017). A fourth-order super-Gaussian temporal profile is used. For these parameters, (4.1) indicates

https://doi.org/10.1017/S0022377822001131 Published online by Cambridge University Press

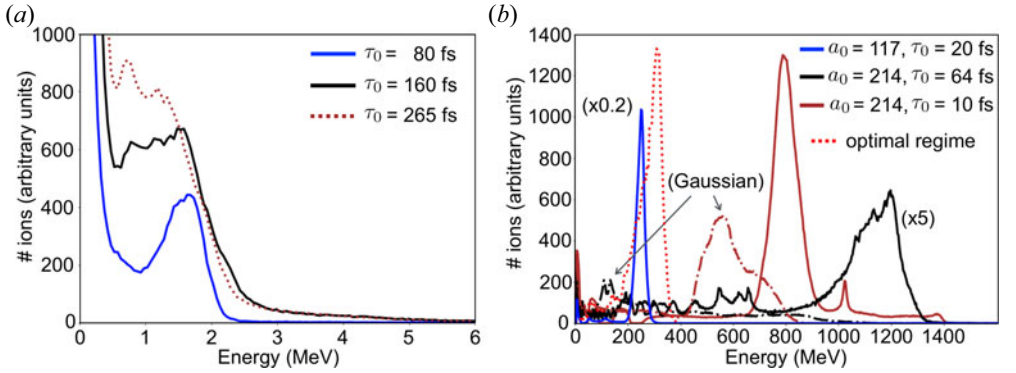

FIGURE 10. Proton energy spectra from 3-D simulations of an intense 1 μm CP laser irradiating an overdense hydrogen target at normal incidence ($\theta_0 = 0^\circ$) for different pulse durations. (*a*) Results for HB regime with laser $a_0 = 12$ and $w_0 = 2$ μm and target $n_0 = 40n_c$ and $l_0 = 3.5$ μm, after the proton beam has left the target rear surface ($t \simeq 310$ fs). (*b*) Results for LS regime with laser $a_0 = 214$ (brown, black) and $a_0 = 117$ (blue), plane wave (solid) or Gaussian transverse profile with $w_0 = 7$ μm (dash–dotted), and target $n_0 = 100n_c$ and $l_0 = 350$ nm, at $t \simeq 2\tau_0$. The dotted red curve shows the spectrum for a $\tau_0 = 15$ fs laser satisfying (7.1): $a_0 = \hat{a}_0 = 122$, with $n_0 = 250n_c$. All the spectra are measured within a 10° opening angle from the laser propagation direction at $t \simeq 2\tau_0$.

$\tau_0 \lesssim 160$ fs for high-quality proton beams to be produced. We thus run three simulations with pulse durations of $\tau_0 = 80$, 160 and 265 fs to test this criterion. In figure 10(*a*), we show the energy spectra of the proton beams exiting the target from the rear surface for these three cases. When the pulse duration is smaller than the predicted threshold, a quasimonoenergetic proton beam is generated, peaking at roughly 1.8 MeV, which corresponds to $v_i = 2v_{\mathrm{HB}} \simeq 0.031c$ and is consistent with (2.1) for $R \simeq 1$. When the pulse duration is comparable to the threshold, we observe that the ion spectral peak at similar energy is still visible, but less prominent. For the longer pulse duration ($\tau_0 = 265$ fs) we find substantial electron heating ($T_e \simeq 3$ MeV), and a strong TNSA field is generated at the rear surface, which broadens the proton energy spread. No clear spectral peak is observed at the same energy. These results confirm the validity of the derived limit on pulse duration for HB based on the development of surface corrugations and associated electron heating.

We note that the generation of narrow energy spread HB ion beams with similar peak energies around 1 MeV have been reported in Palmer *et al.* (2011), where the laser pulse duration appears to meet the criterion of our model. Specifically, they considered a CP CO_2 laser with $\lambda_0 = 10$ μm, $a_0 \simeq 0.7$, $w_0 = 70$ μm and a hydrogen gas jet target with $n_0 \lesssim 10n_c$, $l_0 \sim 800$ μm. The pulse duration used $\tau_0 \simeq 6$ ps was less than $\hat{\tau}_{0,\mathrm{RTI}} \simeq 9$ ps as required by (4.1). The measured ion beam energies were also shown to be consistent with efficient HB.

For the LS regime, additional 3-D simulations have also been performed to illustrate the change in the ion beam quality for different pulse durations. We simulate a CP laser impinging on a planar electron–proton target with $n_0 = 100n_c$ and $l_0 = 350$ nm at normal incidence. The laser pulse is temporally Gaussian and the transverse profile is either Gaussian with $w_0 \simeq 7$ μm or plane wave. These parameters are similar to those used in Qiao *et al.* (2009), where the generation of a GeV proton beam was obtained in 2-D simulations and it was argued that extreme laser intensities were needed to obtain stable high-quality ion beams. Two cases were illustrated: unstable acceleration with $a_0 = 117$

https://doi.org/10.1017/S0022377822001131 Published online by Cambridge University Press

and a stable regime with $a_0 = 214$. Under these conditions, (4.1) predicts that high-quality proton beams require $\tau_0 \lesssim 20$ fs for $a_0 = 117$ and $\tau_0 \lesssim 10$ fs for $a_0 = 214$, both of which are much smaller than the duration $\tau_0 \simeq 64$ fs used in the cited work.

Figure 10(*b*) shows the comparison of the proton spectra at the same time as figure 4 in Qiao *et al.* (2009), which corresponds to $t \simeq 2\tau_0$ after the laser interaction. For the case with $a_0 = 117$, when a pulse duration $\tau_0 = 20$ fs is used, we observe the generation of a high-quality proton beam with 250 MeV, $\Delta\epsilon/\epsilon_0 \simeq 13\,\%$. For the same parameters but using $\tau_0 = 64$ fs (not shown) we observe the generation of a beam with 460 MeV, $\Delta\epsilon/\epsilon_0 \simeq 32\,\%$, similar to their green curve. This indicates that it is the onset of electron heating associated with the surface instability in the longer pulse that leads to the increase of the energy spread and to a significant reduction of the coupling efficiency.

For the highest intensity case ($a_0 = 214$), we observe that similarly the proton beam energy spread is improved from $\Delta\epsilon/\epsilon_0 = 20\,\%$ with $\tau_0 = 64$ fs to $\Delta\epsilon/\epsilon_0 = 12\,\%$ with $\tau_0 = 10$ fs. We further observe that for a transverse Gaussian laser profile the importance of the short pulse duration is even more dramatic. Defining the laser-to-proton energy conversion efficiency η as the fraction of the laser energy being carried by the beam within a 10° opening angle, for $\tau_0 = 10$ fs we obtain high-quality proton beams with $\sim$600 MeV, $\Delta\epsilon/\epsilon_0 = 30\,\%$ and $\eta = 27\,\%$, whereas with $\tau_0 = 64$ fs, we have $\sim$100 MeV, $\Delta\epsilon/\epsilon_0 = 45\,\%$ and $\eta = 0.5\,\%$. The proton beam energy obtained with the short pulse ($\tau_0 = 10$ fs) is comparable to the prediction from 1-D theory of 700 MeV (see (2.3*a*,*b*)). We note that this is slightly higher than the prediction of (7.2) because the target thickness considered in Qiao *et al.* (2009) was $l_0 \lesssim l_{\rm opt}$. More importantly, these results confirm that the process that controls the stability and spectral quality of the LS accelerated ion beams is the electron heating via the development of RTI at the target surface and that choosing the appropriate pulse duration and laser intensity is critical for the acceleration of high-quality ion beams.

Figure 10(*b*) also includes the results of a 3-D PIC simulation for which the laser and target parameters satisfy the optimal LS regime (see (7.1)). We have chosen a set of parameters relevant for near-future short-pulse laser facilities, where a Gaussian laser pulse profile with $\tau_0 = 15$ fs, $w_0 = 5$ μm and $a_0 = \hat{a}_0 \simeq 122$ according to (7.1) is used. The target has $n_0 = 250 n_c$ and $l_0 = l_{\rm opt}$. Under this optimal regime, we indeed observe stable acceleration of the protons via LS leading to the generation of a narrow energy spread proton beam with peak energy $\epsilon_0 \simeq 310$ MeV in very good agreement with the prediction of (7.2), $\Delta\epsilon/\epsilon_0 \simeq 25\,\%$ and $\eta \simeq 2\,\%$. The total laser-to-proton energy conversion efficiency into 4π is $\sim 20\,\%$.

9. Conclusions

In summary, we have presented a detailed study of electron heating and ion acceleration in the interaction of intense laser pulses with overdense plasmas, with a particular focus on radiation pressure acceleration. We have shown that electron heating controls the interplay between different ion acceleration mechanisms. For circularly polarized lasers, the onset of strong electron heating is dominated by the development of corrugations of the target surface on the scale of the laser wavelength due to the laser-driven RTI. In the HB regime, electron heating leads to the development of a collisionless shock and the transition to CSA and TNSA. In the LS regime, electron heating causes fast target expansion and onset of relativistic transparency leading to a significant increase of the ion energy spread. We have shown that to reduce or suppress electron heating and obtain high-quality (low energy spread) ion beams by RPA it is critical to use laser pulses much shorter than the saturation time of the RTI. Using 2-D and 3-D PIC simulations, we have demonstrated that when such short pulses are used high-quality proton beams can be produced with maximum energy

https://doi.org/10.1017/S0022377822001131 Published online by Cambridge University Press

comparable to the optimal 1-D RPA theory, even for lasers with Gaussian transverse and temporal intensity profiles.

Interestingly, we note that a few of the previous experimental studies that reported low energy spread ion beams from either the HB (Palmer *et al.* 2011) or LS (Henig *et al.* 2009; Steinke *et al.* 2013) acceleration appear to meet the laser duration criteria developed in this work. This is encouraging and the understanding provided by our work can help guide future experimental developments in this area. For example, for the parameters of high-power, high-contrast state-of-the-art and near future laser systems with $\tau_0 \simeq 15$ fs, such as the ELI-NP (Doria *et al.* 2020), Apollon 10 PW (Papadopoulos *et al.* 2016) and EP-OPAL (Bromage *et al.* 2019) facilities, our 3-D PIC simulations demonstrate the possibility to produce ∼300 MeV proton beams with ∼25 % energy spread and high coupling efficiency.

Acknowledgements

The authors thank the OSIRIS Consortium, consisting of UCLA and IST (Portugal) for the use of the OSIRIS 4.0 framework and the visXD framework. Simulations were performed at Cori (NERSC) and Theta (ALCF) through ERCAP and ALCC computational grants.

Editor L.O. Silva thanks the referees for their advice in evaluating this article.

Declaration of interest

The authors report no conflict of interest.

Funding

This work was supported by the United States Department of Energy SLAC contract no. DEAC02-76SF00515, by the United States DOE Early Career Research Program under FWP 100331 and by the DOE FES under FWP 100182.

REFERENCES

ANTICI, P., FAZI, M., LOMBARDI, A., MIGLIORATI, M., PALUMBO, L., AUDEBERT, P. & FUCHS, J. 2008 Numerical study of a linear accelerator using laser-generated proton beams as a source. *J. Appl. Phys*. **104** (12), 124901.

AYMAR, G., *et al.* 2020 LhARA: the laser-hybrid accelerator for radiobiological applications. *Front. Phys*. **8**, 567738.

BIN, J.H., *et al.* 2015 Ion acceleration using relativistic pulse shaping in near-critical-density plasmas. *Phys. Rev. Lett*. **115**, 064801.

BORGHESI, M., *et al.* 2002 Electric field detection in laser-plasma interaction experiments via the proton imaging technique. *Phys. Plasmas* **9** (5), 2214–2220.

BORGHESI, M., MACKINNON, A.J., CAMPBELL, D.H., HICKS, D.G., KAR, S., PATEL, P.K., PRICE, D., ROMAGNANI, L., SCHIAVI, A. & WILLI, O. 2004 Multi-MeV proton source investigations in ultraintense laser-goil interactions. *Phys. Rev. Lett*. **92** (5), 4.

BROMAGE, J., *et al.* 2019 Technology development for ultraintense all-OPCPA systems. *High Power Laser Sci. Engng* **7**, e4.

BRUNEL, F. 1987 Not-so-resonant, resonant absorption. *Phys. Rev. Lett*. **59** (1), 52–55.

BULANOV, S.S., *et al.* 2008 Accelerating protons to therapeutic energies with ultraintense, ultraclean, and ultrashort laser pulses. *Med. Phys*. **35** (5), 1770–1776.

BULANOV, S.V., ECHKINA, E.Y., ESIRKEPOV, T.Z., INOVENKOV, I.N., KANDO, M., PEGORARO, F. & KORN, G. 2010 Unlimited ion acceleration by radiation pressure. *Phys. Rev. Lett*. **104** (13), 135003.

BULANOV, S.V., WILKENS, J.J., ESIRKEPOV, T.Z., KORN, G., KRAFT, G., KRAFT, S.D., MOLLS, M. & KHOROSHKOV, V.S. 2014 Laser ion acceleration for hadron therapy. *Phys. Uspekhi* **57** (12), 1149.

https://doi.org/10.1017/S0022377822001131 Published online by Cambridge University Press

CAHILL, A.D., ROSENZWEIG, J.B., DOLGASHEV, V.A., TANTAWI, S.G. & WEATHERSBY, S. 2018 High gradient experiments with X -band cryogenic copper accelerating cavities. *Phys. Rev. Accel. Beams* **21** (10), 102002.

CHOU, H.-G.J., GRASSI, A., GLENZER, S.H. & FIUZA, F. 2022 Radiation pressure acceleration of high-quality ion beams using ultrashort laser pulses. *Phys. Rev. Res*. **4** (2), L022056.

COWAN, T.E., *et al.* 2004 Ultralow emittance, multi-MeV proton beams from a laser virtual-cathode plasma accelerator. *Phys. Rev. Lett*. **92** (20), 204801.

CURRY, C.B., SCHOENWAELDER, C., GOEDE, S., KIM, J.B., REHWALD, M., TREFFERT, F., ZEIL, K., GLENZER, S.H. & GAUTHIER, M. 2020 Cryogenic liquid jets for high repetition rate discovery science. *J. Vis. Exp*. **2020** (159), 61130.

DAIDO, H., NISHIUCHI, M. & PIROZHKOV, A.S. 2012 Review of laser-driven ion sources and their applications. *Rep. Prog. Phys*. **75** (5), 056401.

DENAVIT, J. 1992 Absorption of high-intensity subpicosecond lasers on solid density targets. *Phys. Rev. Lett*. **69** (21), 3052–3055.

DOLLAR, F., *et al.* 2012 Finite spot effects on radiation pressure acceleration from intense high-contrast laser interactions with thin targets. *Phys. Rev. Lett*. **108**, 175005.

DORIA, D., CERNAIANU, M.O., GHENUCHE, P., STUTMAN, D., TANAKA, K.A., TICOS, C. & UR, C.A. 2020 Overview of ELI-NP status and laser commissioning experiments with 1 PW and 10 PW class-lasers. *J. Instrum*. **15** (9), C09053.

DROMEY, B., *et al.* 2016 Picosecond metrology of laser-driven proton bursts. *Nat. Commun*. **7** (1), 1–6.

ELIASSON, B. 2015 Instability of a thin conducting foil accelerated by a finite wavelength intense laser. *New J. Phys*. **17** (3), 33026.

ESIRKEPOV, T., BORGHESI, M., BULANOV, S.V., MOUROU, G. & TAJIMA, T. 2004 Highly efficient relativistic-ion generation in the laser-piston regime. *Phys. Rev. Lett*. **92** (17), 175003.

FIUZA, F., STOCKEM, A., BOELLA, E., FONSECA, R.A., SILVA, L.O., HABERBERGER, D., TOCHITSKY, S., GONG, C., MORI, W.B. & JOSHI, C. 2012 Laser-driven shock acceleration of monoenergetic ion beams. *Phys. Rev. Lett*. **109** (21), 215001.

FIUZA, F., STOCKEM, A., BOELLA, E., FONSECA, R.A., SILVA, L.O., HABERBERGER, D., TOCHITSKY, S., MORI, W.B. & JOSHI, C. 2013 Ion acceleration from laser-driven electrostatic shocks. *Phys. Plasmas* **20** (5), 56304.

FONSECA, R.A., MARTINS, S.F., SILVA, L.O., TONGE, J.W., TSUNG, F.S. & MORI, W.B. 2008 One-to-one direct modeling of experiments and astrophysical scenarios: pushing the envelope on kinetic plasma simulations. *Plasma Phys. Control. Fusion* **50** (12), 9.

FONSECA, R.A., SILVA, L.O., TSUNG, F.S., DECYK, V.K., LU, W., REN, C., MORI, W.B., DENG, S., LEE, S., KATSOULEAS, T. & ADAM, J.C. 2002OSIRIS: a three-dimensional, fully relativistic particle in cell code for modeling plasma based accelerators. In *Computational Science – ICCS 2002: International Conference Amsterdam, The Netherlands, April 21–24, 2002 Proceedings, Part III* (ed. P.M.A. Sloot, A.G. Hoekstra, C.J. Kenneth Tan & J.J. Dongarra), pp. 342–351. Springer.

FONSECA, R.A., VIEIRA, J., FIUZA, F., DAVIDSON, A., TSUNG, F.S., MORI, W.B. & SILVA, L.O. 2013 Exploiting multi-scale parallelism for large scale numerical modelling of laser wakefield accelerators. *Plasma Phys. Control. Fusion* **55** (12), 124011.

GAMALY, E.G. 1993 Instability of the overdense plasma boundary induced by the action of a powerful photon beam. *Phys. Rev.* E **48** (4), 2924–2928.

GAUTHIER, M., *et al.* 2017 High repetition rate, multi-MeV proton source from cryogenic hydrogen jets. *Appl. Phys. Lett*. **111** (11), 114102.

GIBBON, P. 2005 *Short Pulse Laser Interactions with Matter*. Imperial College Press and distributed by World Scientific Publishing Co.

GÖDE, S., *et al.* 2017 Relativistic electron streaming instabilities modulate proton beams accelerated in laser-plasma interactions. *Phys. Rev. Lett*. **118** (19), 194801.

GRASSI, A., GRECH, M., AMIRANOFF, F., MACCHI, A. & RICONDA, C. 2017 Radiation-pressure-driven ion Weibel instability and collisionless shocks. *Phys. Rev.* E **96** (3), 33204.

GRECH, M., SKUPIN, S., DIAW, A., SCHLEGEL, T. & TIKHONCHUK, V.T. 2011 Energy dispersion in radiation pressure accelerated ion beams. *New J. Phys*. **13** (12), 123003.

HABERBERGER, D., TOCHITSKY, S., FIUZA, F., GONG, C., FONSECA, R.A., SILVA, L.O., MORI, W.B. & JOSHI, C. 2012 Collisionless shocks in laser-produced plasma generate monoenergetic high-energy proton beams. *Nat. Phys*. **8** (1), 95–99.

HENIG, A., *et al.* 2009 Radiation-pressure acceleration of ion beams driven by circularly polarized laser pulses. *Phys. Rev. Lett*. **103** (24), 245003.

HIGGINSON, A., *et al.* 2018 Near-100 MeV protons via a laser-driven transparency-enhanced hybrid acceleration scheme. *Nat. Commun*. **9** (1), 724.

KAR, S., *et al.* 2012 Ion acceleration in multispecies targets driven by intense laser radiation pressure. *Phys. Rev. Lett*. **109** (18), 185006.

KHUDIK, V., YI, S.A., SIEMON, C. & SHVETS, G. 2014 The analytic model of a laser-accelerated plasma target and its stability. *Phys. Plasmas* **21** (1), 013110.

KIM, I.J., *et al.* 2016 Radiation pressure acceleration of protons to 93 MeV with circularly polarized petawatt laser pulses. *Phys. Plasmas* **23** (7), 070701.

KIM, J.B., GÖDE, S. & GLENZER, S.H. 2016 Development of a cryogenic hydrogen microjet for high-intensity, high-repetition rate experiments. *Rev. Sci. Instrum*. **87** (11), 11E328.

KLIMO, O., PSIKAL, J., LIMPOUCH, J. & TIKHONCHUK, V.T. 2008 Monoenergetic ion beams from ultrathin foils irradiated by ultrahigh-contrast circularly polarized laser pulses. *Phys. Rev. Accel. Beams* **11** (3), 31301.

KRAFT, S.D., *et al.* 2010 Dose-dependent biological damage of tumour cells by laser-accelerated proton beams. *New J. Phys*. **12** (8), 085003.

KROLL, F., *et al.* 2022 Tumour irradiation in mice with a laser-accelerated proton beam. *Nat. Phys*. **18** (3), 316–322.

KRUER, W.L. & ESTABROOK, K. 1985 JxB heating by very intense laser light. *Phys. Fluids* **28** (1), 430–432.

LINZ, U. & ALONSO, J. 2016 Laser-driven ion accelerators for tumor therapy revisited. *Phys. Rev. Accel. Beams* **19** (12), 124802.

LOEFFLER, J.S. & DURANTE, M. 2013 Charged particle therapy - optimization, challenges and future directions. *Nat. Rev. Clin. Oncol*. **10** (7), 411–424.

MACCHI, A. & BENEDETTI, C. 2010 Ion acceleration by radiation pressure in thin and thick targets. *Nucl. Instrum. Meth. Phys. Res. Sec.* A **620** (1), 41–45.

MACCHI, A., BORGHESI, M. & PASSONI, M. 2013 Ion acceleration by superintense laser-plasma interaction. *Rev. Mod. Phys*. **85** (2), 751–793.

MACCHI, A., CATTANI, F., LISEYKINA, T.V. & CORNOLTI, F. 2005 Laser acceleration of ion bunches at the front surface of overdense plasmas. *Phys. Rev. Lett*. **94** (16), 165003.

MACCHI, A., GRASSI, A., AMIRANOFF, F. & RICONDA, C. 2019 Momentum absorption and magnetic field generation by obliquely incident light. *Eur. Phys. J. Plus* **134** (9), 420.

MACCHI, A., VEGHINI, S. & PEGORARO, F. 2009 'Light Sail' acceleration reexamined. *Phys. Rev. Lett*. **103** (8), 085003.

MAY, J., TONGE, J., FIUZA, F., FONSECA, R.A., SILVA, L.O., REN, C. & MORI, W.B. 2011 Mechanism of generating fast electrons by an intense laser at a steep overdense interface. *Phys. Rev.* E **84** (2), 025401.

MCILVENNY, A., *et al.* 2021 Selective ion acceleration by intense radiation pressure. *Phys. Rev. Lett*. **127**, 194801.

MORA, P. 2003 Plasma expansion into a vacuum. *Phys. Rev. Lett*. **90** (18), 185002.

OBST, L., *et al.* 2017 Efficient laser-driven proton acceleration from cylindrical and planar cryogenic hydrogen jets. *Sci. Rep*. **7** (1), 10248.

PAK, A., *et al.* 2018 Collisionless shock acceleration of narrow energy spread ion beams from mixed species plasmas using 1 μm lasers. *Phys. Rev. Accel. Beams* **21**, 103401.

PALMER, C.A.J., *et al.* 2012 Rayleigh-Taylor instability of an ultrathin foil accelerated by the radiation pressure of an intense laser. *Phys. Rev. Lett*. **108** (22), 225002.

PALMER, C.A.J., DOVER, N.P., POGORELSKY, I., BABZIEN, M., DUDNIKOVA, G.I., ISPIRIYAN, M., POLYANSKIY, M.N., SCHREIBER, J., SHKOLNIKOV, P., YAKIMENKO, V. & NAJMUDIN, Z. 2011 Monoenergetic proton beams accelerated by a radiation pressure driven shock. *Phys. Rev. Lett*. **106** (1), 14801.

https://doi.org/10.1017/S0022377822001131 Published online by Cambridge University Press

PAPADOPOULOS, D.N., *et al.* 2016 The apollon 10 pw laser: experimental and theoretical investigation of the temporal characteristics. *High Power Laser Sci. Engng* **4**, e34.

PARADKAR, B.S. & KRISHNAGOPAL, S. 2016 Electron heating in radiation-pressure-driven proton acceleration with a circularly polarized laser. *Phys. Rev.* E **93** (2), 023203.

PATEL, P., MACKINNON, A., KEY, M., COWAN, T., FOORD, M., ALLEN, M., PRICE, D., RUHL, H., SPRINGER, P. & STEPHENS, R. 2003 Isochoric heating of solid-density matter with an ultrafast proton beam. *Phys. Rev. Lett*. **91** (12), 125004.

PEGORARO, F. & BULANOV, S.V. 2007 Photon bubbles and ion acceleration in a plasma dominated by the radiation pressure of an electromagnetic pulse. *Phys. Rev. Lett*. **99** (6), 065002.

QIAO, B., ZEPF, M., BORGHESI, M. & GEISSLER, M. 2009 Stable GeV ion-beam acceleration from thin foils by circularly polarized laser pulses. *Phys. Rev. Lett*. **102** (14), 145002.

ROBINSON, A.P.L., ZEPF, M., KAR, S., EVANS, R.G. & BELLEI, C. 2008 Radiation pressure acceleration of thin foils with circularly polarized laser pulses. *New J. Phys*. **10** (1), 013021.

ROTH, M., *et al.* 2001 Fast ignition by intense laser-accelerated proton beams. *Phys. Rev. Lett*. **86** (3), 436–439.

RYGG, J.R., *et al.* 2008 Proton radiography of inertial fusion implosions. *Science* **319** (5867), 1223–5.

SCULLION, C., *et al.* 2017 Polarization dependence of bulk ion acceleration from ultrathin foils irradiated by high-intensity ultrashort laser pulses. *Phys. Rev. Lett*. **119**, 054801.

SENTOKU, Y., MIMA, K., KOJIMA, S. & RUHL, H. 2000 Magnetic instability by the relativistic laser pulses in overdense plasmas. *Phys. Plasmas* **7** (2), 689–695.

SGATTONI, A., SINIGARDI, S., FEDELI, L., PEGORARO, F. & MACCHI, A. 2015 Laser-driven Rayleigh-Taylor instability: plasmonic effects and three-dimensional structures. *Phys. Rev.* E **91** (1), 13106.

SGATTONI, A., SINIGARDI, S. & MACCHI, A. 2014 High energy gain in three-dimensional simulations of light sail acceleration. *Appl. Phys. Lett*. **105** (8), 84105.

SHEN, X.F., QIAO, B., PUKHOV, A., KAR, S., ZHU, S.P., BORGHESI, M. & HE, X.T. 2021 Scaling laws for laser-driven ion acceleration from nanometer-scale ultrathin foils. *Phys. Rev.* E **104** (2), 025210.

SILVA, L.O., MARTI, M., DAVIES, J.R., FONSECA, R.A., REN, C., TSUNG, F.S. & MORI, W.B. 2004 Proton shock acceleration in laser-plasma interactions. *Phys. Rev. Lett*. **92** (1), 15002.

SNAVELY, R.A., *et al.* 2000 Intense high-energy proton beams from petawatt-laser irradiation of solids. *Phys. Rev. Lett*. **85** (14), 2945–2948.

STEINKE, S., HILZ, P., SCHNÜRER, M., PRIEBE, G., BRÄNZEL, J., ABICHT, F., KIEFER, D., KREUZER, C., OSTERMAYR, T., SCHREIBER, J., ANDREEV, A.A., YU, T.P., PUKHOV, A. & SANDNER, W. 2013 Stable laser-ion acceleration in the light sail regime. *Phys. Rev. Accel. Beams* **16** (1), 011303.

TAHIR, N.A., *et al.* 2005 Proposal for the study of thermophysical properties of high-energy-density matter using current and future heavy-Ion accelerator facilities at GSI Darmstadt. *Phys. Rev. Lett*. **95** (3), 035001.

VARMAZYAR, P., MIRZANEJHAD, S. & MOHSENPOUR, T. 2018 Effect of pre-plasma on the ion acceleration by intense ultra-short laser pulses. *Laser Part. Beams* **36** (2), 226–231.

WAGNER, F., *et al.* 2016 Maximum proton energy above 85 MeV from the relativistic interaction of laser pulses with micrometer thick CH_2 targets. *Phys. Rev. Lett*. **116** (20), 205002.

WAN, Y., *et al.* 2016 Physical mechanism of the transverse instability in radiation pressure ion acceleration. *Phys. Rev. Lett*. **117** (23), 234801.

WAN, Y., ANDRIYASH, I.A., LU, W., MORI, W.B. & MALKA, V. 2020 Effects of the transverse instability and wave breaking on the laser-driven thin foil acceleration. *Phys. Rev. Lett*. **125** (10), 104801.

WAN, Y., PAI, C.H., ZHANG, C.J., LI, F., WU, Y.P., HUA, J.F., LU, W., JOSHI, C., MORI, W.B. & MALKA, V. 2018 Physical mechanism of the electron-ion coupled transverse instability in laser pressure ion acceleration for different regimes. *Phys. Rev.* E **98** (1), 013202.

WANG, T., KHUDIK, V. & SHVETS, G. 2021 Laser-ion lens and accelerator. *Phys. Rev. Lett*. **126** (2), 024801.

WILKS, S.C. & KRUER, W.L. 1997 Absorption of ultrashort, ultra-intense laser light by solids and overdense plasmas. *IEEE J. Quant. Electron*. **33** (11), 1954–1968.

WILKS, S.C., KRUER, W.L., TABAK, M. & LANGDON, A.B. 1992 Absorption of ultra-intense laser pulses. *Phys. Rev. Lett*. **69** (9), 1383–1386.

WILKS, S.C., LANGDON, A.B., COWAN, T.E., ROTH, M., SINGH, M., HATCHETT, S., KEY, M.H., PENNINGTON, D., MACKINNON, A. & SNAVELY, R.A. 2001 Energetic proton generation in ultra-intense laser–solid interactions. *Phys. Plasmas* **8** (2), 542–549.

WU, D., ZHENG, C.Y., QIAO, B., ZHOU, C.T., YAN, X.Q., YU, M.Y. & HE, X.T. 2014 Suppression of transverse ablative Rayleigh-Taylor-like instability in the hole-boring radiation pressure acceleration by using elliptically polarized laser pulses. *Phys. Rev.* E **90** (2), 023101.

YU, T.-P., PUKHOV, A., SHVETS, G. & CHEN, M. 2010 Stable laser-driven proton beam acceleration from a two-ion-species ultrathin foil. *Phys. Rev. Lett*. **105** (6), 065002.

YU, T.P., PUKHOV, A., SHVETS, G., CHEN, M., RATLIFF, T.H., YI, S.A. & KHUDIK, V. 2011 Simulations of stable compact proton beam acceleration from a two-ion-species ultrathin foil. *Phys. Plasmas* **18** (4), 043110.

ZHOU, M.L., YAN, X.Q., MOUROU, G., WHEELER, J.A., BIN, J.H., SCHREIBER, J. & TAJIMA, T. 2016 Proton acceleration by single-cycle laser pulses offers a novel monoenergetic and stable operating regime. *Phys. Plasmas* **23** (4), 043112.

https://doi.org/10.1017/S0022377822001131 Published online by Cambridge University Press